SPIN-DYNAMICS IN COLD GASES OF 87Rb AND ATOMIC HYDROGEN

The spins they are a-changin'

by

Otto Vainio

From

Department of Physics and Astronomy
University of Turku
Finland

Supervised by

Kalle-Antti Suominen   Sergei Vasiliev
Professor   Docent
Department of Physics and Astronomy Department of Physics and Astronomy
University of Turku   University of Turku
Finland   Finland

Reviewed by

Matti Krusius   Yuriy Bunkov
Professor   Professor
O.V. Lounasmaa Laboratory   Institut Neel
Aalto University   CNRS
Finland   France

Opponent

David Lee
Professor
Department of Physics and Astronomy
Texas A&M University
USA

Kun itse tekee, saa juuri sellaisen kuin sattuu tulemaan.

- pikkuveli

Acknowledgments

My journey towards the fulfilment of requirements for this thesis has been a long one. And during a long journey one has a chance to meet many people; many wonderful people. I definitely have.

It all started with the open-minded encouragement by my supervisor Kalle-Antti Suominen and accepting me as an experimental physics student despite the fact that the actual experiments were literally on the other side of the world. In addition to the scientific mentoring I very much appreciate your ever positive attitude and also the fact that there has been a constant funding for me, no matter how tight the situation has been. Thank you.

The other side of the world, the University of Queensland, Australia, more precisely in my case, was an utterly enjoyable place to work at. For that I'll express my warmest thanks to Halina Rubinsztein-Dunlop, Norman Heckenberg, Chris Vale and Matthew Davis. I have learned so much from you it's hard to believe I didn't spend more time down under. I also wish to thank the whole physics community at UQ for the friendly and welcoming atmosphere which made both work and leisure a joy.

Back at my home university, the University of Turku, I first of all want to thank my second supervisor Sergei Vasiliev. Working with the atomic hydrogen experiment under your guidance has been a pleasure. Despite the difficult technical challenges and sometimes stupefying physics, your relentless and inspiring search for solutions and gentle supervision has made the work very rewarding.

I have also been very lucky with regard to the other important aspect of support, the peer support. Thank you Kari Härkönen and Janne Ahokas for the stress relieving conversations as well as the academic collaboration and co-authorship. There's a real danger I would have ended up as a premature curmudgeon without you.

Thank you Jyrki and Sabrina for enlivening "the corridor". You brought with you an incredibly wit and fun bunch of people, with whom the everyday work became a luxury. Thank you Janika, Laura, Ruggero, Pinja, Elsi, Kimmo and all the other previous and more recent colleagues.

I also want to thank the technical support from the university workshops, both here in Turku and at UQ. Your skills and know-how are one of the key elements required for building setups for experimental physics.

The studies is of course not all there is to life. During a project as long as mine the other side life has to be taken seriously too. I wish to thank my parents Eeva and Olli for all sorts support, e.g. the tailored financial aid

packages that have been very helpful. Thank you little brothers Eero and Pekko for not taking me too seriously and therefore reminding what the really important stuff is. Thank you Kaarina and Rainer for your "24/7" help and support.

My heartiest thanks to my dear wife Paula for the love and support you gave me especially during the times of writing when I was suffering from the serious symptoms neither described by Upper[a], nor later explained by Didden et al.[b]. Kiitos Niilolle äärimmäisen tehokkaasta ajatusten toisaalle saattamisesta. Se tuli usein tarpeeseen, tilattuna tai ilman.

Lastly, I would like to thank Jenny and Antti Wihuri Foundation and The Finnish Cultural Foundation for financial support.

[a]Dennis Upper. The unsuccessful self-treatment of a case of "writer's block". *Journal of Applied Behavior Analysis*, 7:497, 1974

[b]R. Didden, J. Sigafoos et al. A multisite cross-cultural replication of Upper's (1974) unsuccessful self-treatment of writer's block, *Journal of Applied Behavior Analysis*, 40:773, 2007

Contents

Abstract

In this thesis the dynamics of cold gaseous atoms is studied. Two different atomic species and two different experimental techniques have been used.

In the first part of the thesis experiments with Bose-Einstein condensates of ^{87}Rb are presented. In these experiments the methods of laser cooling and magnetic trapping of atoms were utilized. An atom chip was used as the experimental technique for implementation of magnetic trapping. The atom chip is a small integrated instrument allowing accurate and detailed manipulation of the atoms.

The experiments with ^{87}Rb probed the behaviour of a falling beam of atoms outcoupled from the Bose-Einstein condensate by electromagnetic field induced spin flips. In the experiments a correspondence between the phases of the outcoupling radio frequency field and the falling beam of atoms was found.

In the second part of the thesis experiments of spin dynamics in cold atomic hydrogen gas are discussed. The experiments with atomic hydrogen are conducted in a cryostat using a dilution refrigerator as the cooling method. These experiments concentrated on explaining and quantifying modulations in the electron spin resonance spectra of doubly polarized atomic hydrogen. The modifications to the previous experimental setup are described and the observation of electron spin waves is presented. The observed spin wave modes were caused by the identical spin rotation effect. These modes have a strong dependence on the spatial profile of the polarizing magnetic field. We also demonstrated confinement of these modes in regions of strong magnetic field and manipulated their spatial distribution by changing the position of the field maximum.

List of articles

This thesis consists of an introductory review and the following five articles:

I   O. Vainio, C. J. Vale, M. J. Davis, N. R. Heckenberg
and H. Rubinsztein-Dunlop
Fringe spacing and phase of interfering matter waves
Physical Review A 73, 063613 (2006) (6 pages)

II   K. Härkönen, O. Vainio and K.-A. Suominen
*Wave-packet analysis of interference patterns in output
coupled atoms*
Physical Review A 81, 043638 (2010) (7 pages)

III   M. C. Garrett, A. Ratnapala, E. D. van Ooijen, C. J. Vale,
K. Weegink, S. K. Schnelle, O. Vainio, N. R. Heckenberg,
H. Rubinsztein-Dunlop and M. J. Davis
*Growth dynamics of a Bose-Einstein condensate in a dimple trap
without cooling*
Physical Review A 83, 013630 (2011) (9 pages)

IV   J. Ahokas, O. Vainio, S. Novotny, J. Järvinen and S. Vasiliev
*Magnetic resonance line shifts in the quantum gas of
atomic hydrogen*
Physica Scripta T140, 014012 (2010) (5 pages)

V   O. Vainio, J. Ahokas, S. Novotny, S. Sheludyakov, D. Zvezdov,
K.-A. Suominen and S. Vasiliev
*Guiding and trapping of electron spin waves in atomic
hydrogen gas*
Physical Review Letters 108, 185304 (2012) (5 pages)

Chapter 1

Introduction

The fundamental concept behind quantum physics is that everything happens in discrete steps. For every change in every system there are always discrete states between which the changes happen. This is however not what we experience when we observe the everyday world around us. We see smooth transitions instead of abrupt or graduated changes. The seemingly continuous flow of the world around us follows from the unimaginably large number of these quantum states and their interactions involved in even the tiniest of events we can perceive.

If we want to test the predictions of quantum physics we need to simplify the system we are going measure. We need to limit the number of available states. One way of doing this is to lower the temperature of the system we are going to study. A prime example of this is the phenomenon of Bose-Einstein condensation in which a single quantum state is occupied by millions of atoms. In cold temperatures, i.e. systems with low energies, also the wave particle dualism of matter becomes a prominent feature of the system.

The wave nature of matter was studied in the experiments conducted with ^{87}Rb described in chapter 2. The experiments were done in the atom optics laboratory in the University of Queensland, in Brisbane, Australia.

Lowering the temperature also affects the way atoms interact with each other. For example, at low enough temperatures only certain types of scatterings between atoms in a gaseous sample are possible. Under appropriate conditions these limitations have macroscopic influence on the behaviour of the sample.

In chapter 3 experiments with atomic hydrogen gas conducted at the University of Turku are presented. In these experiments, in addition to bringing out quantum characteristics of the interactions, the low tempera-

ture in its part allows stabilizing a spin polarized gaseous sample of atomic hydrogen against recombination to molecules. As hydrogen is the simplest of elements, a single electron circling around a single proton, it is also a good testing ground for theories. Especially because the interaction potentials can be accurately calculated from the theory.

In the experiments with atomic hydrogen the dynamics of the electron spin were studied. The quantum mechanical spin is a fundamental characteristic of the quantum state of a particle. For the first time collective excitations called spin waves of electron spin were observed.

Chapter 2

Studies with ^{87}Rb Bose-Einstein condensates

2.1 Brief introduction BEC and atom laser experiments

2.1.1 From first BEC observations to atom lasers

The first Bose-Einstein condensates (BEC) were observed in dilute gases of alkali metals in 1995 [1, 2, 3], seventy years after theoretical prediction by Einstein [4, 5] based on findings by S. N. Bose [6]. This achievement was the onset of a whole new field of experimental quantum physics. A BEC is a macroscopic entity being comprised of millions of atoms, but because all the atoms in a BEC occupy the same quantum state, the collective behaviour of these atoms follow the time evolution of a single wave function.

From an experimental point of view, a BEC can therefore be seen as a bridge over the gap between classical and quantum physics. By observing the dynamics of a Bose-Einstein condensate the effects of quantum physics can in many occasions be detected in a single measurement rather than building an ensemble via numerous repetitions. An example is the probing of the phase coherence properties of a BEC, which were among the early condensate experiments [7, 8] and theoretical analyses [9, 10]. The long coherence length of a BEC naturally renders the possibility for experimenting with the wave-nature of matter, which was postulated by de Broglie in 1925 [11] and for the first time experimentally confirmed using electrons in [12].

2.1.2 Atom laser experiments, a brief review

Relatively soon after the first successful BEC experiments it was estimated that by outcoupling atoms from this coherent source pulses and beams of atoms, i.e. matter waves, with long coherence lengths could be generated [13, 14, 15]. In an analogy to the traditional photon laser, the BEC acts as the cavity and the chosen method of outcoupling works as the semi-transparent mirror. Therefore quite appropriately, the coherent outcoupled beam of atoms falling under gravity is often referred to as an atom laser. The first experimental demonstration of an atom laser based on a BEC is described in reference [16]. Very soon after this initial observation other experiments utilizing various techniques followed [17, 18]. Simultaneously also the theory of atom lasers was advancing [19, 20, 21, 22, 23]. In the first atom laser experiments the outcoupling process was more or less pulsed, but in 1999 Bloch et al. demonstrated an atom laser with continuous outcoupling [24] and soon after they used the technique with a dual frequency rf field to measure the spatial coherence of a condensate [25]. The results were theoretically analysed in reference [26].

During the first years of the new millennium several other atom optical experiments with atom lasers followed [27, 28, 29, 30, 31, 32]. Even though the outcoupling in these experiments was already continuous, the duration of the outcoupling was still limited due to the fact that the size of the condensate was finite. In 2008 Robins et al. for the first time demonstrated a pumped atom laser in an experiment where the BEC used as the atom laser cavity was fed from another, spatially separate condensate [33]. During the same year an atom laser was also used for probing another condensate [34].

2.1.3 The experimental technique: an atom chip

The gaseous alkali BEC experiments have since the beginning utilized the experimental methods of laser cooling, magnetic trapping, and often detection by imaging the cloud of atoms with a laser pulse and a CCD camera. The gaseous BEC experiments have to be implemented in free space, or more accurately in a vacuum as good as technically feasible, and therefore only magnetic field minima can be used for trapping the atoms.

In the first magneto-optical traps (MOT) for neutral atoms [35] the six orthogonal cooling and trapping laser beams crossed in free space inside the vacuum chamber and the magnetic field minimum for final trapping was created with macroscopic coils. In these setups the experiment cycle times were long and further manipulation of the BEC was challenging.
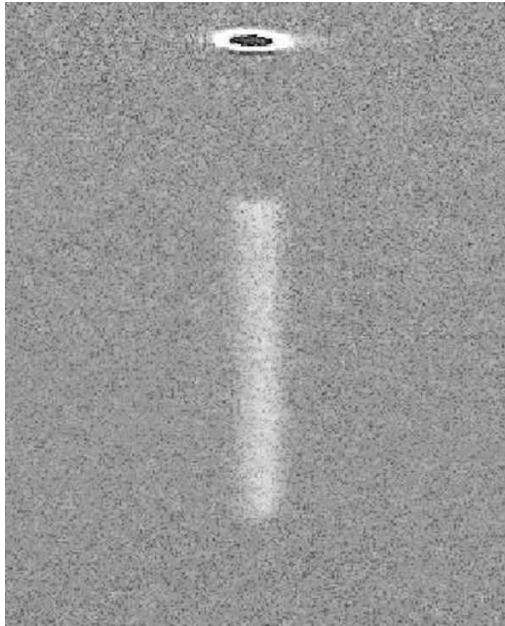
Figure 2.1: Absorption image of an atom laser beam and the condensate it originated from. A weak outcoupling field has been on for several milliseconds producing a steady stream of atoms from the BEC. Consequently, after a short break with zero outcoupling and a few milliseonds before imaging, the condensate has been released from the trap. The data for this image is recorded by the author in the atom optics laboratory of the University of Queensland.

Microscopic traps for neutral atoms had been suggested already in 1995 [36] and cold atoms had been manipulated with microelectronics before [37, 38, 39, 40, 41, 42], but it was in 2001 when Hänsel et al. [43] and Ott et al. [44] showed that it was possible to create a BEC using micro-fabricated current carriers on the surface of a substrate. These planar current carrier structures, aka. atom chips allowed the creation of steeper magnetic field gradients and curvatures, and therefore tighter traps, as the field minimum used for trapping was brought closer to the current carrier. The geometry of the trap is a very important factor in achieving a gaseous alkali BEC because of the density (n) dependence of the key parameter, the phase-space density $\rho = n\Lambda^3$. The other factor, the thermal de Broglie wavelength

Λ, is related to the temperature as $1/\sqrt{T}$. In addition to offering more favourable conditions for BEC creation, the promising versatility of atom chips as experimental tools for matter waves was demonstrated in 2002 in a proposal for a matter wave interferometer [45] and in an experiment with a magnetic waveguide on an atom chip [46]. During the same year already, reviews on the subject were published [47, 48], followed later by e.g. [49] and even an entire book dedicated to atom chips [50].

The small distance between the trapped atoms and material surfaces including the current carrying wires introduces its own set of challenges, some of them predicted already in 1999 by Henkel et al. [51, 52] and later further analysed in references [53, 54]. Simultaneously experiments with cold gases and BECs were successfully conducted in microtraps, not only confirming the existence of surface induced perturbations [55, 56, 57, 58, 59], but also showing that the decoherence and fragmentation problems could be overcome by refining experimental techniques [60, 61, 62, 63, 64, 65], including the realization [66, 67, 68] and theoretical analysis [69] of superconductive atom chips.

Towards the end of the first decade of the 21st century more and more sophisticated experiments utilizing atom chips were conducted. These include mounting an optical cavity on the atom chip [70], studying the coherence dynamics of 1D quasi-condensates [71], atom chips with microwave wave-guides [72], an atom chip with optical fibre for single atom detection [73], using an atom chip for studies of spin-squeezing and entanglement [74] and recently a study of Hanbury Brown and Twiss correlations across the Bose-Einstein condensation threshold [75].

2.2   Our experiments

The atom chip used in the experiments for **paper I** is described in more detail in reference [76] and the rest of the experimental setup in reference [77].

2.2.1   Magneto-optical trap, pre-cooling

The particular MOT used in the experiments done for **paper I** was a mirror-MOT, where two of the six orthogonal laser beams are replaced by reflections from a mirror. In this setup the mirror was a silver foil, into which the conductors needed for the creation of magnetic trapping

potential were machined. The initial magneto-optical trapping and cooling happened therefore near the surface of the atom chip.
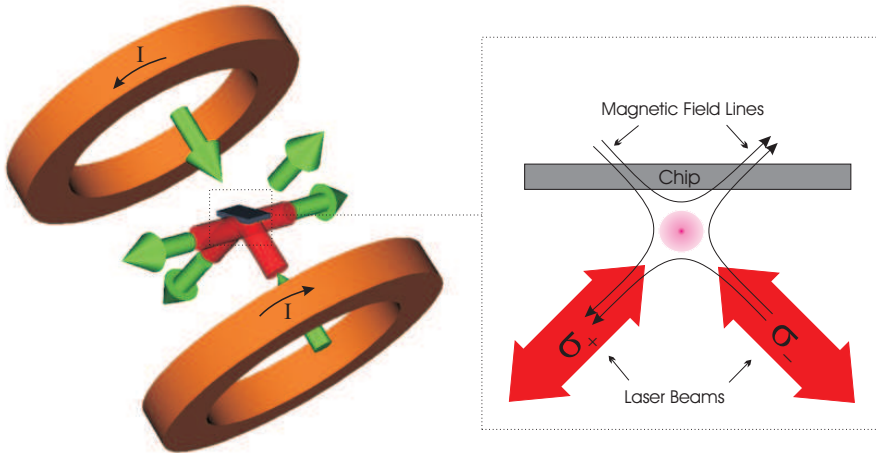

Figure 2.2: Laser alignment and the magnetic field of the anti-Helmholtz coils in a mirror-MOT. Figure from reference [78].

2.2.2 Magnetic wire trap, final cooling

The final stage of trapping in the atom laser experiments for **paper I** were performed by utilizing magnetic forces only. A spatially inhomogeneous magnetic field exerts a force on an atom with a reasonably strong magnetic moment μ, according to $\mathbf{F} = \nabla(\mu \cdot \mathbf{B})$.

In contrast to the quadrupole field of a MOT created with coils in anti-Helmholtz configuration, the local field minimum in a wire trap is produced as the sum of a uniform field created by Helmholtz coils and a field due to a current carrying wire. The wire is positioned perpendicular to the Helmholtz field and these two fields will exactly cancel each other at a certain distance from the wire. In addition to these two fields an extra bias field, perpendicular to the trapping Helmholtz field, is introduced in order to prevent losses from the trap due to Majorana spin flips [79, 80]. It is the magnitude of this extra field that defines the resonance conditions for the transitions between the Zeeman sub-states.

Because of the small size of the BEC it is sufficient to characterise the trap as a harmonic potential, even if the macroscopic profile of the magnetic field magnitude is certainly not parabolic. In atom chip experi-

ments utilizing a wire trap, due to the geometry of the trapping wire, the magnetic field minimum is often very elongated, resulting in cigar-shaped condensates. By tuning the currents, regimes ranging from nearly one-dimensional quasi-condensates [81] all the way to fully phase coherent 3D condensates can be generated.

Once the pre-cooled cloud of atoms is loaded into this purely magnetic trap further cooling is achieved by a method called evaporative cooling [82]. In forced evaporative cooling the highest energy atoms are selectively flipped to non-trapping magnetic states by a radio frequency field.

Magnetic trap details

The wire-trap with a "Z" configuration, as described in e.g. [37], provided an elongated, or cigar-shaped, field minimum with trapping frequencies around 6-7 Hz in axial direction and up to ≈ 1000 Hz in the radial. In the experiments a radial trapping frequency between ≈ 100 and 500 Hz was usually chosen in order to avoid fragmenting of the BEC due to small spatial separation from the imperfect conductors. Also, with high aspect ratios the one-dimensionality of the BEC starts to have a strong influence on the phase coherence of the condensate.

Because a fully phase coherent 3D condensate was preferred for the outcoupling experiments, a final stage trap with axial frequency 6.7 Hz and radial frequency 160 Hz was chosen.

2.2.3 RF outcoupling

The same setup for the radio frequency field used for evaporative cooling during the preparation stage of the experiment can also be used for energy-selective outcoupling from within the BEC. While outcoupling, the rf field frequency is simply tuned to resonance with the bottom of the trap where the BEC is, rather than to a higher frequency, as with evaporative cooling.

2.2.4 Detection

An often used method for detecting the BEC is time-of-flight imaging. In this method the trapped cloud of atoms is released from the trap and after a short period of ballistic flight it is imaged with a short laser pulse and a CCD array. This method of imaging is destructive, i.e. the BEC is lost after each detection. The ballistic flight is usually needed for expanding the cloud since trapped BECs are, while macroscopic compared to single

atoms, still too small ($\approx 1\mu$m) to be imaged directly without special arrangements. After ballistic expansion only modest magnification is needed before imaging.

In outcoupling experiments a ballistic expansion also provides the important time resolution, as the distance the outcoupled atoms have travelled after leaving the BEC directly corresponds to the amount of time that has passed since the outcoupling took place.

During ballistic expansion the kinetic energy distribution of the trapped cloud starts to affect the imaged spatial distribution. The shape of the detected cloud depends on the time delay between releasing the atoms and recording the image. Apart from an initial kick due to repulsive atom-atom interactions within the condensate, the only force affecting the atoms in an atom laser is gravity.

The method used for imaging the cloud of atoms in the experiments described in **paper I** is called absorptive imaging. In absorptive imaging a weak resonant laser beam is directed through the BEC straight towards the CCD array and a 2D shadow of the atomic cloud is recorded. By properly selecting the laser power, exposure time, and CCD sensitivity the atomic density can be accurately extracted from the luminance data within the shadow area.

2.2.5   Choice of atomic species

Because of its favourable physical properties [83] ^{87}Rb has been widely used in BEC experiments from the beginning [1]. As with all the other alkalis, it is the single outer electron that defines the level structure and corresponding electric and magnetic interactions available for experimental manipulation.

The energy separation between the two fine structure levels, $5^2S_{1/2}$ and $5^2P_{3/2}$ corresponds an optical wavelength of $\approx$ 780 nm, which is experimentally convenient due to readily available diode lasers.

Of the two hyperfine levels of the ground state $5^2S_{1/2}$, corresponding to total spins $F = 1$ and $F = 2$, $F = 1$ was utilized in the experiment. In a magnetic field this state further splits into three magnetic (Zeeman) substates, of which the state with $m_f = -1$ is a low field seeker and therefore trappable in a magnetic field minimum. The state with $m_f = 1$ is a high field seeker and is therefore repelled from the magnetic field minimum and atoms ending up on it are usually not seen during detection. In an atom laser it is the atoms on the sub-state with $m_f = 0$ that fall freely under gravity and form the coherent matter wave beam.

2.2.6 Atom laser experiments

The experiments described in **paper I** were inspired by the beautiful results of I. Bloch et al. described in reference [25]. The aim of the study was to examine in more detail the relationship between a dual frequency outcoupling rf field and the resulting interference pattern of the matter waves.

The two subjects of special interest were how the phase and beat frequency of the interfering matter waves relate to the phase and frequency difference between the outcoupling rf fields.

In order to be able to directly compare the behaviour of outcoupled atoms to the temporal distribution of the outcoupling rf field amplitude, the vertical spatial axis of the absorption images were scaled according to $t_z = \sqrt{2(z - z_0)/g}$, as shown in figure 3 of **paper I**.

Through the analysis of the results it became clear that the beat frequency and the phase difference of the interfering matter wave beams matched exactly those of the outcoupling rf fields. This is a very reasonable outcome from the point of view of energy conservation.

2.2.7 Theoretical analysis and numerical simulations

In **paper II** the outcoupling scenario with weak single and dual frequency rf outcoupling was studied using a wave-packet method. It was shown that the wave-packets consisting of uncountable sets of individually unphysical eigenstates (Airy functions) can accurately and meaningfully present a physical solution.

In addition to the analytical results presented in **paper II** the outcoupling scenario was simulated numerically in one spatial dimension for the three Zeeman sub-states $m_f = -1, 0, +1$. The scaled equations of motion for the three states involved are:

$$i\frac{\partial \psi_1(z,t)}{\partial t} = -\frac{1}{2}\nabla^2 \psi_1 + \left(V_1 + g_{int}\left|\psi\right|^2\right)\psi_1 + \frac{\Omega_{rf}\psi_2}{\sqrt{2}} \tag{2.1}$$

$$i\frac{\partial \psi_2(z,t)}{\partial t} = -\frac{1}{2}\nabla^2 \psi_2 + \left(V_2 + g_{int}\left|\psi\right|^2\right)\psi_2 + \frac{\Omega_{rf}\psi_1}{\sqrt{2}} + \frac{\Omega_{rf}\psi_3}{\sqrt{2}} \tag{2.2}$$

$$i\frac{\partial \psi_3(z,t)}{\partial t} = -\frac{1}{2}\nabla^2 \psi_3 + \left(V_3 + g_{int}\left|\psi\right|^2\right)\psi_3 + \frac{\Omega_{rf}\psi_2}{\sqrt{2}} \tag{2.3}$$

Here g_{int} is the scaled 1D contact interaction term, Ω_{rf} the Rabi frequency related to the coupling rf field and V_1, V_2 and V_3 are the harmonic trapping

potential, linear gravitational potential and harmonic anti-trapping potential, accordingly. $|\psi|^2 = |\psi_1|^2 + |\psi_2|^2 + |\psi_3|^2$ is the total density. The simulations were run for both interacting and noninteracting ($g_{int} = 0$) cases. Because of the finite spatial grid in the simulations, absorptive boundary conditions were introduced within the potentials V_1, V_2 and V_3 by adding imaginary components to the ends of the grid. The initial state for the simulations was calculated using the imaginary time evolution method. The match between the analytical solutions on the simulations was very good, as presented in figure 7 of **paper II**. In figure 8 simulation results with g_{int} corresponding to 10^5 ^{87}Rb atoms in the given potential are shown. While these results qualitatively provide a match between the analytical results and simulations with $g_{int} = 0$, clear differences are also visible, especially at the beginning and end of the outcoupled stream of atoms. The simulations were implemented with XMDS [84], which provided both an easy human readable scripting language and fast and error free code for the computation.

2.2.8   Studies of condensate formation in a dimple trap

Even though there has been a multitude of experiments with Bose-Einstein condensates ever since the first observations in 1995, the understanding of the full dynamics of condensate formation has been less than complete. Already in 1998 Miesner et al. conducted experiments showing signs of bosonic stimulation within the formation [85]. Later experiments probing the onset of a BEC include e.g. observing the formation of long-range order by Ritter et al. [86] and population and phase coherence growth by Hugbart et al. [87].

In **paper III** the dynamics of condensate formation is studied. Instead of lowering the temperature of the sample by evaporative cooling in a fixed potential below the critical temperature to form a condensate, the cooling was stopped just before reaching the transition temperature. Consequently the shape of the trapping potential was changed in order to increase the phase-space density enough to form a partial condensate, as previously described by Stamper-Kurn et al. [88]. The idea of adiabatically changing the phase-space density of Bose gases was already introduced before with spin polarized atomic hydrogen by Pinkse et al. [89]. The additional trapping potential (dimple) was created by introducing a tightly focused, far red-detuned, laser crossing the magnetically trapped cloud of cold atoms perpendicular to the weak trapping dimension. The final trap where the
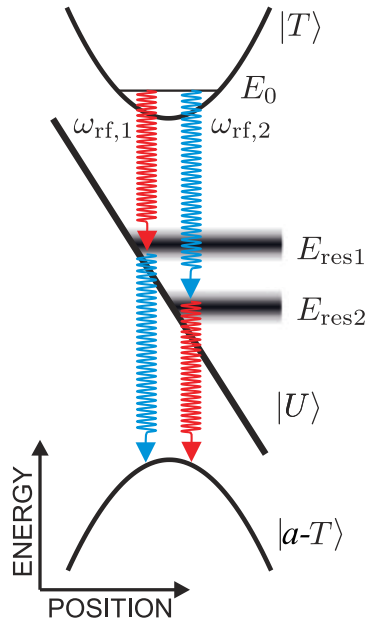
Figure 2.3: Schematic of the potentials for the three magnetic sub-states labeled as $|T\rangle$, $|U\rangle$ and $|a\text{-}T\rangle$ for the trapped, untrapped (free-falling) and anti-trapped (expelled by the magnetic field) states. The two outcoupling rf fields $\omega_{rf,1}$ and $\omega_{rf,2}$ define resonance energies E_{res1} and E_{res2} in the untrapped state. The same rf fields also couple the free-falling states to anti-trapped sub-states ($m_f = 1$).

BEC was formed was therefore a combination of a magnetic atom chip trap and an optical dipole trap [90]. Similar technique, albeit with all-optical trapping, has been used to create Cs condensates by Weber et al. [91]. Because the optical elements for the dipole trap were not incorporated into the atom chip but were located outside the vacuum chamber, changing the trapping parameters, i.e. the width of the focal point, was relatively easy allowing experiments with various trap geometries. This combined use of built-in micro-manipulation techniques within the sealed vacuum chamber and external adjustable optics serves, for its part, as an example of the growing complexity of the experimental setups necessary for modern quantum physics experiments.
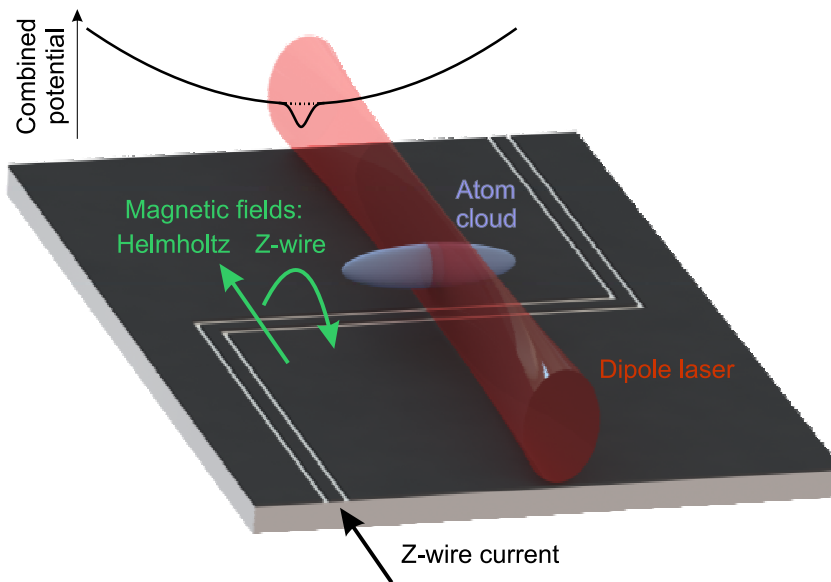
Figure 2.4: Schematic view of the atom cloud in a Z-wire magnetic trap, the laser beam for the optical dipole trap and the potential produced as a combination of these trapping techniques. In the real experiment the atom cloud is "hanging" below the chip.

Chapter 3

Spin waves in atomic hydrogen

3.1 Background

3.1.1 Motivation: unexplained disturbances

The motivation for the electron spin wave experiments was to further our understanding of the phenomenon that was causing the peculiar line shapes during the previous experiments on the clock shift, discussed in **paper IV** and in reference [92]. The modulation of the absorption and dispersion signals due to these assumed spin wave peaks was under certain circumstances limiting the accuracy of the line shift measurements. Therefore a more detailed study was planned.

3.1.2 Two kinds of interactions

At the beginning of the spin wave experiment analyses two different spin transfer mechanisms were considered as the possible sources for the modulations in the spectra:

1. Spin waves due to long range dipolar interaction which are also known as magnetostatic, or Walker, modes [93, 94, 95].

2. Spin waves due to the exchange interaction, also referred to as the identical spin rotation effect (ISRE) [96, 97, 98].

The magnetostatic modes can be understood in classical terms as a result of the magnetic dipole-dipole coupling between the spins. In a magnetized medium excited with an inhomogeneous rf field this coupling can

result in spatial modulations in the magnetization, which in turn cause modulations within the ESR spectrum.

The identical spin rotation effect, in contrast, is fundamentally a quantum phenomenon, as it is a direct consequence of the (in)distinguishability of the colliding atoms in binary collisions.

Even though the underlying physics behind these two spin transfer mechanisms are different, they can, under appropriate conditions, lead to similar structures in the recorded spectra. It was only after analysing various experimental scenarios that conclusive evidence about the nature of certain types of modulations in the spectra measured in our experiments was found.

3.1.3   Magnetostatic spin waves

The history of magnetostatic spin waves dates back to the year 1956 when White et al. [93] and Dillon et al. [99] reported their experiments on ferromagnetic resonance in ferrites. Soon after Mercereau and Feynman [94] and L. R. Walker [95] provided theoretical explanation for the multiple resonances seen in these experiments with spheroidal samples.

In his article Walker showed that by making the magnetostatic approximation

$$\boldsymbol{\nabla} \times \mathbf{H} = 0 \tag{3.1}$$

$$\boldsymbol{\nabla} \cdot \mathbf{B} = 0 \tag{3.2}$$

it followed from the Landau-Lifshitz equation

$$\frac{d\mathbf{M}}{dt} = \gamma_e \left(\mathbf{M} \times \mathbf{H}\right) \tag{3.3}$$

that there were standing wave solutions of the magnetization according to the wave equation

$$\left(\lambda_i \left(\frac{\partial^2}{\partial x^2} + \frac{\partial^2}{\partial y^2}\right) + \frac{\partial^2}{\partial z^2}\right) \Psi_i = 0 \tag{3.4}$$

within the magnetized sample induced by the external rf field. The structure and frequency of these magnetostatic modes depends only on the shape, size and saturation magnetization of the sample. The equations will be explained in more detail in section 3.3.5.

In 1960 it was also recognized by Eshbach and Damon [100] that in addition to the modulations within the volume of the magnetized medium,

there were modes concentrating on the surface of the magnetized sample, and that the full magnetostatic spin wave spectrum was the combination of these. In addition to the special case of a spherical sample considered in the early studies, in the early 1960s the theory of the resonances and propagation characteristrics of magnetostatic waves were studied in other geometries [101, 102, 103, 104, 105, 106], as the shape and size of the sample as well as the direction of magnetization are the key elements defining the magnetostatic Walker mode spectrum. Later more detailed analyses of the magnetostatic modes have been carried out, especially in the field of solid state physics of thin film structures, e.g. references [105, 107, 108], because of the important applications in microwave signal processing and magnetic recording devices. Another somewhat more recent experiment with magnetostatic waves is the observation of magnetostatic modes in solid ^{3}He [109].

Other more recent examples of magnetostatic spin wave studies include the utilization of variational calculus, finite element method, and other computational tools in the analysis [110, 111, 112]. Also, there has been studies incorporating both dipole and exchange spin waves within the same analysis [113].

3.1.4   Spin waves in quantum gases

Identical spin rotation spin waves in gases

The identical spin rotation effect becomes important as a source of collective spin excitations in the regime of quantum gases, in which the de Broglie wavelength of the atoms exceeds the (hard sphere) scattering length of the atom, but the system is not necessarily degenerate.

As is concisely explained in e.g. the references [114, 115, 116], the ISRE can be briefly summarized as follows: The wave function of a particle with a spin that is tilted from the quantization axis (due to an exciting rf field) has components of both parallel (with the magnetic field) and anti-parallel spins. In a collision these two components will acquire different phase shifts depending on the amplitude differences of the corresponding components of the other colliding particle. This follows from the fact that the quantum mechanical scattering process between indistinguishable particles (alike components) is different compared to the scattering process between unidentical particles (components with opposite spins). The general effect of these phase shifts is the rotation of the spins of both of the colliding particles around the sum of the combined total spin. The total spin of

the colliding particles is preserved in the process. Cumulatively these spin-rotation events can lead to the propagation of ISR spin waves, i.e. collective excitations, again resulting in modulations in the measured spectra.

The onset of identical spin rotation effect spin waves in dilute gases took place in the beginning of 1980s when Lhuillier and Laloë introduced the concept of ISRE in reference [97] and derived the equation for the spin orientation current based on it [98]. They deliberately used a notation matching to the equation Leggett had previously derived for the spin density in liquid ^{3}He [117] to emphasize the similarity, even if the origins of the important coefficients (the dimensionless quality factor μ and spin diffusion constant D_0) were explained in a slightly different manner. The linearized approximation of this hydrodynamic equation of motion for the transversal magnetization in the rotating frame as presented in [117] (and in relevance to hydrogen experiments, but with slightly differing terms in the appendix of [114]) is

$$\frac{\partial S_+}{\partial t} = \frac{D_0(1 - i\mu\epsilon S_z)}{1 + \mu^2 S^2}\nabla^2 S_+ + \gamma\delta H_0 S_+ \tag{3.5}$$

where, in addition to μ and D_0, S and S_z are a measure of the spin-polarization, ϵ is $+1$ for bosons and -1 for fermions, γ is the gyromagnetic ratio, δH_0 is the magnetic field deviation from its average value and

$$S_+ = S_x + iS_y \tag{3.6}$$

where S_x and S_y are the components of the transversal magnetization in spin space. The first prediction of spin waves in quantum gases was actually by Bashkin in 1981 [96], but he did not use the concept of ISRE.

A little later in a third article Lhuillier calculated in more detail the phase shifts during collisions in ^{3}He and in spin polarized hydrogen and deuterium [118]. The first observations of ISRE spin waves followed soon after in gaseous ^{3}He [119, 120], ^{3}He -^{4}He mixture [121] and H↓[122]. Already in 1984 Lévy and Ruckenstein provided a quasiparticle description [123] to these spin oscillations emphasizing the connection to the molecular field description previously used with degenerate Fermi liquids, such as liquid ^{3}He. They also considered the phenomenon of Bose-Einstein condensation of these quasiparticles. Other theoretical investigations that followed included the detailed analysis of ISRE spin waves in various regimes with atomic hydrogen [114], consideration of 2D spin waves in atomic hydrogen adsorbed on a superfluid ^{4}He film [124] and a study of hydrodynamic properties of magnetization oscillations [125]. At the end of the decade a

more detailed experiment of the nuclear spin waves in atomic hydrogen was published by Bigelow et al. [126] showing that the waves survive even in the Knudsen regime.

After a hectic decade during the eighties there was a relatively quiet period in gaseous ISRE spin wave research. A new wave of ISRE spin wave studies started in 2001 when Lewandowski et al. conducted an experiment with ^{87}Rb , using the experimental methods of laser cooling and magnetic trapping, in which they detected an "anomalous spin-state segregation" [127]. The results were almost instantaneously explained as being ISRE induced by three separate groups [128, 129, 130], shortly followed by another experimental spin wave study by the same group [131]. In 2008 Du et al. also observed an "anomalous spin segregation", this time in a Fermi gas of ^{6}Li [132] and again theoretical explanations followed rapidly [133, 134]. In a 2009 article Du et al. reported results about controlling the spin current in ^{6}Li [135]. Other recent studies involving ISRE induced spin transport include a study of spin self-rephasing by Deutsch et al. [136], and two other experimental studies by McGuirk et al. [137, 138].

Spin waves in liquid ^{3}He

Another system where spin waves have been studied is liquid ^{3}He. In liquid ^{3}He the spin transfer phenomena are explained by means of a molecular field [117], a mean field method, the fundamental origin of which lies in the quantum mechanical exchange interaction. Only two years later, in 1972, Corruccini et al. reported measurements of spin waves in liquid ^{3}He systems [139]. The next spin wave experiments were reported more than ten years later [140, 141, 142], when also the interesting observation of homogeneously precessing domain (HPD) was reported [143, 144]. The HPD was later identified as a Bose-Einstein condensation of magnons by Bunkov and Volovik [145, 146]. A magnon is a quantized spin wave, a quasiparticle.

Summary

Altogether exchange interaction spin waves have been studied in six different systems. These are listed in table 3.1. In terms of equation (3.5) there are four parameters affecting the behaviour of this type of spin waves: D_0, ϵ, μ and γ.

The first term, D_0, is the spin diffusion coefficient in unpolarized gas and the effect of the difference between fermions and bosons through ϵ

Regime	ϵ	μ	γ
^{3}He - liquid	-1	n/a	$-$
^{3}He - gas	-1	$-/+$	$-$
H↓ - nuclear	$+1$	$-$	$+$
H↓ - electron	$+1$	$-$	$-$
^{87}Rb - gas	$+1$	n/a	$-/+$
^{6}Li - gas	-1	n/a	$-/+$

Table 3.1: Exchange interaction spin wave experiments and the signs of the important parameters.

is straightforward. The value of μ, including sign, depends on both temperature and the quantum states involved in the collision. The relevant quantum states again depend on the magnitude of the magnetic field. For example our experiments with doubly polarized hydrogen are conducted in high magnetic field and the electron $\mathbf{S}$ and nuclear $\mathbf{I}$ spins are good quantum numbers independently. As mentioned in section 2.2.5, recent alkali-gas experiments usually utilize reasonably low magnetic fields and therefore a good quantum number describing the atomic states is the total spin $\mathbf{F} = \mathbf{I} + \mathbf{S} + \mathbf{L}$ (where $\mathbf{L}$ is the electron orbital angular momentum). In reference [114] (and references therein) Bouchaud and Lhuillier discuss these two regimes in terms of the hydrogen atom and present the temperature dependent quality factors μ for both hyperfine spin waves (low field), and electronic spin waves (high field). This was possible due to the simplicity of the hydrogen atom (and gaseous helium) as the interaction potentials were known.

The gyromagnetic ratio γ defines the direction and strength of the spin wave response to gradients of the magnetic field. For example the previously detected nuclear spin waves (γ_n is positive) in atomic hydrogen are, borrowing the naming practice used in dilute alkali experiments, "low field seekers", which are effected by the local magnetic field minima as potential wells, as opposed to the eletronic spin waves reported in **paper V**, which are "high field seekers" due to γ_e being negative and react to magnetic field maxima as minima of their potential.

3.2 Experimental apparatus

The experiments with spin polarized atomic hydrogen were done in a cryostat using a dilution refrigerator as the final cooling technique. As with BEC experiments, the purpose of the experimental setup is to cool a sample of gaseous atoms to low enough temperatures allowing experiments in the quantum regime.

In open traps, such as the magneto-optical traps, only the gaseous sample of atoms is cooled and it remains fully thermally insulated from the rest of the experimental apparatus, whereas in a dilution refrigerator the coldest spot of the setup is the mixing chamber, to which the sample is mechanically attached. The fundamental difference between these two methods is that the spin polarized hydrogen gas is in contact with the walls of its container.

This physical contact allows the application of strong compression of the sample gas using liquid helium as piston and consequently very high densities can be reached, compared to alkali BEC experiments.

The experiments described here are another stage in a continuum of experiments conducted over several decades and the relevant changes for the experiments described in this thesis were the construction of a new experimental cell (the functional part inside which the sample is created and manipulated), including a new compression volume and a modified liquid helium level meter for controlling the compressions.

3.2.1 Overview

The main parts of the experimental setup are a cryostat with a dilution refrigerator, a 6 Tesla superconductive magnet, a 128 GHz electron spin resonance (ESR) spectrometer, and equipment for managing hydrogen and fine tuning the magnetic field. The bottom temperature of our self-made dilution refrigerator is 20 mK and its maximum circulation rate is 300 μmoles/second. The high homogeneity superconducting magnet is manufactured by Donetsk Physical-Technical Institute (Ukraine) and it can reach a field of 6 T with a homogeneity of $2 \cdot 10^{-6}$ in 1 cm diameter sphere. The magnet is equipped with a set of shim coils and a sweep coil, each having their own persistent switches allowing individual control.

3.2.2 Changes in the ESR spectrometer circuitry

The main detection method of these experiments is the ESR spectrometer, the construction and operation of which is described in detail in reference [147].

During these experiments the possibility of using pulsed excitation and recording the subsequent free induction decay signal was introduced by adding a SpinCore Technologie Pulse Blaster DDS-II-300 radio frequency pulse generator. In addition to being capable of providing shaped pulses of chosen center frequency the rf generator provides the first intermediate frequency for continuous wave (CW) detection. This arrangement allows switching between pulsed and CW measurements almost instantaneously, and both methods can be used within the same experiment cycle. The components added to the ESR spectrometer circuitry are shown in red in figure 3.1. The pulsed spectra are recorded with an Agilent U1082A (AP240) digitizer capable of 1 GHz sample frequency. The digitizer card is within the computer controlling the experiment, whereas the CW signal is processed with a dual channel lock-in-amplifier before data collection to the computer.

3.2.3 The new experimental cell

The experimental cell, the heart of the apparatus where the final manipulation and probing of the sample gas happens, was redesigned for these experiments. The most significant change within the experimental cell was the fully plastic composition of the sample volume container. The basis for the modifications was the cell with an all-copper construction used in previous experiments, which were reported in **paper IV**. The construction of this first generation compression cell is described in reference [92].

Sample volume, plastic container

The all-plastic sample volume container was machined out of a block of Stycast 1266. The purpose of this choice of material was to minimize the amount of magnetized media around the sample.

The sample volume itself is a thin walled ≈ 6 mm long polyimide (Kapton) tube with an outer diameter of 0.5 mm. It was made out of an insulated copper wire by etching out the copper with nitric acid. One end of the tube was glued perpendicularly to a 12.5 μm thick Kapton foil and a support disc made of Stycast was then glued to the bottom of the foil around the
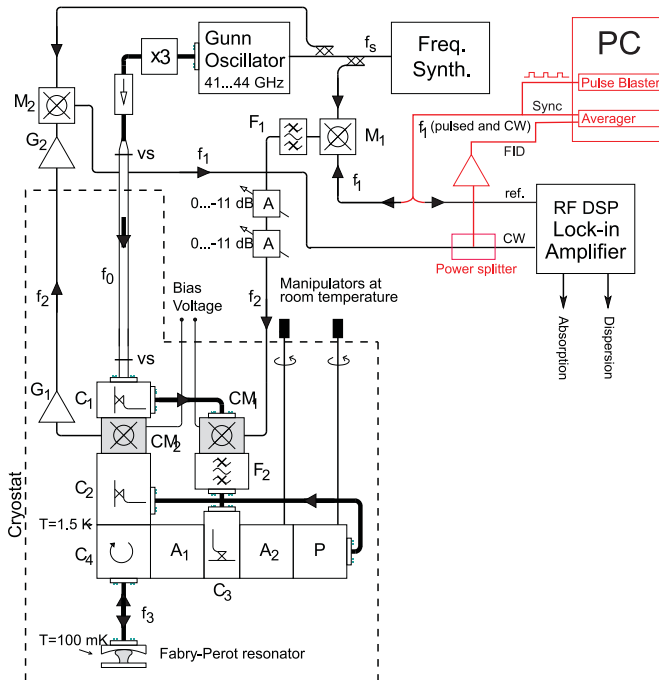
Figure 3.1: Schematic of the 128 GHz ESR spectrometer. The modifications to the setup described in [147], which allow the pulsed recording of free induction decay signals, are drawn in red.

tube. The Kapton foil seals the top of the sample volume. Subsequently this composition was glued to the rest of the container.

Even though the support disc was not originally designed to be in contact with the sample tube, while gluing the support disc a meniscus of Stycast ≈ 0.5 mm in height was formed outside the tube between the tube, the Kapton film, and the Kapton film support disc. This meniscus is shown in figure 3.3.

The Kapton foil surface on top of the container was coated by sputtering with a thin $(1\mu m)$ layer of gold, which serves as the flat mirror of the Fabry-Pérot cavity. In order to couple the hydrogen sample to the cavity field a ≈ 0.4 mm diameter area centered on top of the sample tube was masked before sputtering, thus leaving a sub-critical orifice which allowed an evanescent tail of the ESR field to penetrate to the sample volume inside the Kapton tube. The effective length of the evanescent field was estimated to be $\approx 80\mu m$. With this arrangement a highly inhomogeneous excitation field could be generated. The inhomogeneity of the rf field is one of the
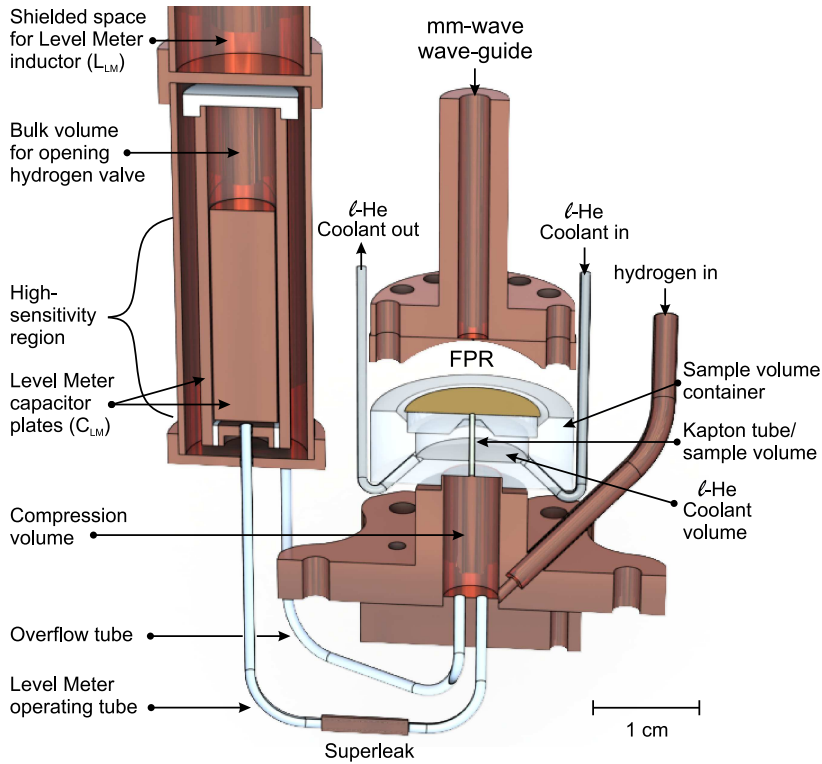
Figure 3.2: The modified experimental cell. Cross-sections of the sample and compression volume, Fabry-Pérot resonator (FPR), capacitive helium level meter, liquid helium coolant volume, and the connecting tubing are shown. The sample volume consisting of a Kapton tube surrounded by liquid helium coolant volume is entirely made of plastic, apart from the gold coating on its top side, acting as the flat mirror of the FPR.

necessary conditions for exciting spin waves.

The space inside the container surrounding the sample tube serves as a liquid helium (l-He) coolant volume and is connected via stainless steel tubes to a heat exchanger bolted to the mixing chamber. The liquid helium coolant was crucial for the success of high compression ratios, reducing overheating due to recombination heat.

Comparison of experimental cell generations

The experimental cell described above and shown in figures 3.2 and 3.3 was the cell used in the spin wave experiments reported in **paper V**. It is the

FPR flat mirror (gold coating on the Kapton foil sealing the end of the Kapton tube)

~0.4 mm hole in the gold coating, coupling the FPR rf field the sample volume

Stycast meniscus

Kapton foil support epoxy (Stycast 1266)

0.5 mm diameter Kapton tube into which the hydrogen is compressed
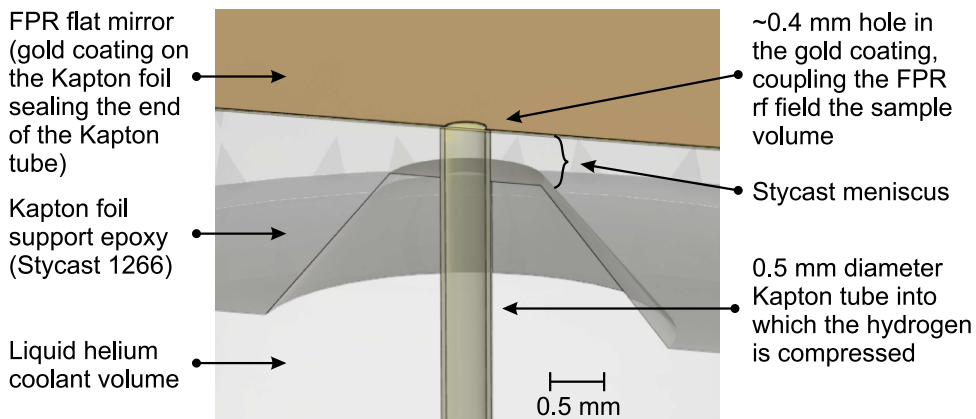
Liquid helium coolant volume

0.5 mm

Figure 3.3: Close-up of the experimental cell.

third compression cell and the second cell with an all-plastic construction.

The first plastic cell suffered from instabilities of the gold coated flat mirror and it had a superleak at the top of the sample volume, preventing efficient use of the liquid helium coolant and accurate density and height measurements of the sample. Importantly though, in this cell there was no Stycast meniscus right next to the sample volume. Similarly to the second plastic cell, the copper cell had also magnetized media in the immediate vicinity of the hydrogen sample. The tops of the sample volumes of these three generations of experimental cells with representative spectra are shown in figure 3.4. The copper cell spectrum and the spectrum recorded with the second plastic cell show features on left from the main absorption peak. The first plastic cell without the meniscus on the contrary never produced data with this second absorption peak. The effect of the magnetization will be discussed in more in detail in section 3.3.4.

Compression volume, pure copper

Below the plastic container is the compression volume into which the atomic hydrogen sample is accumulated in the beginning of each experiment cycle. The part containing the compression volume is machined out of extremely pure copper ($> 99.99\%$ purity) and it is thermally coupled to the mixing chamber via copper rods. The plastic sample volume container is glued around a thin collar of the copper part in order to allow flexing without cracking due to differing coefficients of heat expansion.

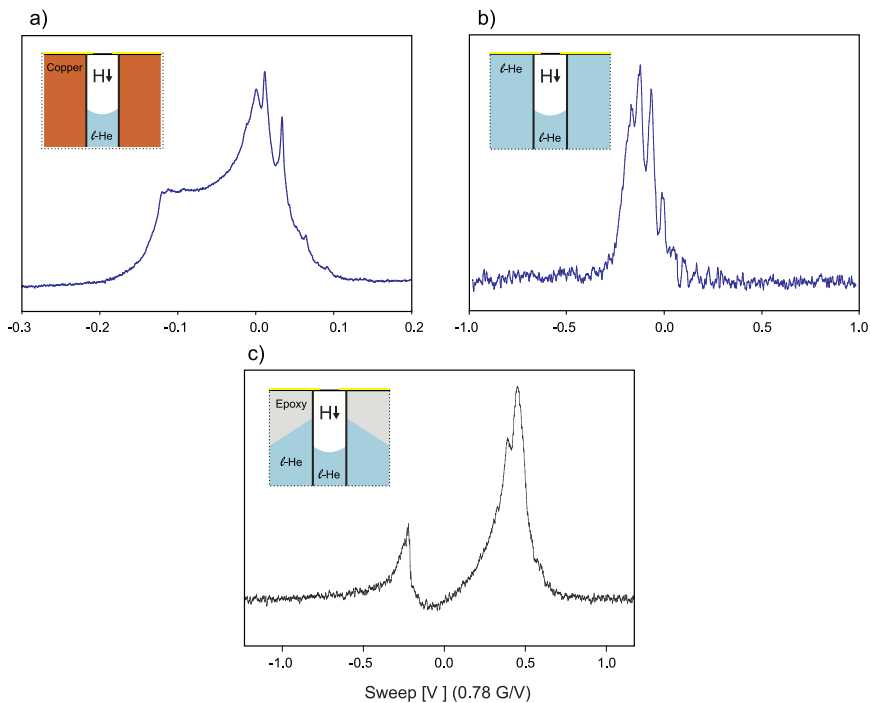The atomic hydrogen sample is accumulated from the dissociator via

Figure 3.4: Spectra recorded with three generations of experimental cells. a) Copper cell b) Plastic cell without stycast meniscus c) Plastic cell with a Stycast meniscus around the sample volume.

the fill line into the compression volume through a small, 0.5 mm diameter hole on the wall close to the bottom.

The temperature of the sample is monitored and controlled with thermally coupled thermometers (RuO_2 thick film chip resistors) on the compression volume. The thermometers were calibrated with a ^{3}He melting curve thermometer in a separate experimental run. The temperature range in our experiments is between ≈ 220 mK and ≈ 650 mK. Most experiments have been conducted at temperatures around 370 mK and 480 mK.

3.2.4 Fountain valve and helium level meter

Contrary to the liquid helium coolant which is located in a separate, isolated volume, the l-He used for compressing the sample is in direct contact with the hydrogen sample, and in fact a thin film of it covers all the walls of the sample and compression volumes.
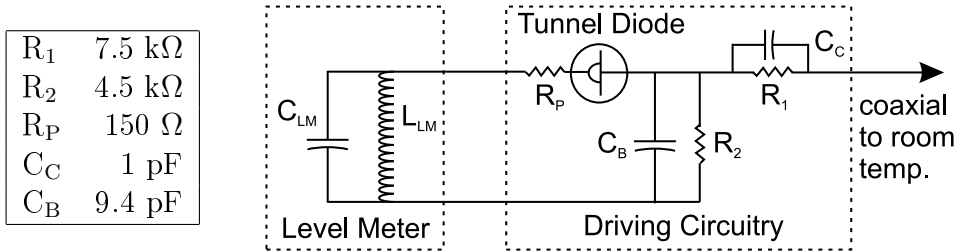
R₁	7.5 kΩ

Figure 3.5: Schematic of the TDO driving circuit and values of components.

The reservoir from which the liquid helium is pumped into the hydrogen volume is also used for measuring the l-He level. This reservoir, also referred to as the level meter, is connected to the bottom of the compression volume through stainless steel piping. Within the piping is a super leak through which only the superfluid part of the helium can penetrate. This construction allows pumping the l-He back and forth between the compression/sample volume and the reservoir by controlling the temperature difference between them. For controlling the temperature, a chip thermometer is connected to the bottom of the level meter, next to the operating tube connection.

Inside the compression volume the l-He works both as the piston compressing the atomic hydrogen gas towards the top of the plastic sample volume and as the valve opening and closing the hydrogen fill line.

Level meter construction

Inside the level meter the l-He is located in the volume between two capacitor plates. The capacitor is connected in parallel with an inductor in order to form an oscillator driven by a tunnel diode oscillator (TDO) circuitry [148, 149]. The approximate range of the values for the components of the driving circuitry followed the suggestions given in reference [148], but the final selection was based on two requirements. Firstly, stable oscillation had to be achieved in the range of a few tens of MHz. Secondly, achieving as low as possible DC power consumption was preferable. The resistors cause a DC power consumption of 10 μW, significantly reducing the heat load compared to the previously used controller. Due to the high sensitivity of the oscillator the final selection procedure was largely trial and error. The chosen values resulting in oscillation at $\approx$ 25 MHz are shown in table 3.5. The accurate values of the inductance of coil L_{LM} and the capacitance of the capacitor C_{LM} are not known.

The level meter doubling as l-He reservoir was also redesigned for these experiments. To improve the accuracy of the level measurement the inner capacitor plate was made out of a 20 mm long solid copper bar with a radius of 2.85 mm, instead of the tube used previously. The modification increased the l-He level change related to the volume of helium pumped between the level meter and the compression volume. The distance between the capacitor plates in this high sensitivity region is 0.15 mm leaving a volume of only 55 mm^3 between the plates.

The frequency difference between empty and full (of liquid helium) capacitor is $\approx$ 190 kHz and with our usual sampling rate of 0.5 Hz the detection accuracy is a few Hertz. This gives a volume resolution of approximately 1 nl corresponding to a helium level change of $\approx$ 0.2 μm in the sample volume. While calculating the helium level changes the cross-sections of the hydrogen fill-line and the helium overflow-tubing have to be taken into account too, as explained in reference [150].

Because of this reduced volume directly between the capacitor plates an extra reservoir was constructed above the inner plate (solid bar) of the capacitor. This reservoir allowed complete emptying of the compression volume and opening of the hydrogen fill line for the accumulation of a new sample.

Both the capacitor C_{LM} and the parallel inductor L_{LM} where fully enclosed in a copper shielding to minimize the effect of external interference.

3.2.5 Magnetic fields

Coils

The magnetic field in the sample volume is a sum of several individual sources. The main magnet creating the $\approx$ 4.6 Tesla polarising field also has a set of linear (Lx, Ly, Lz) and parabolic (Lz^2) shim coils for maximizing the static field homogeneity.

In addition to the built-in coils of the main magnet, three sets of coils wound of a 140 μm diameter superconducting wire were used. Two of these sets of coils were wound around the radiation shield. One of these sets of coils was wound in the Helmholtz configuration (coils separated by their radius R $\approx$ 30 mm) and the other one in the anti-Helmholtz configuration (coils separated by $\sqrt{3}$R).

The coils in Helmholtz configuration allow homogeneous field sweeps and the set in anti-Helmholtz configuration the creation of linear axial field gradients.

The third coil configuration was a single coil located directly on top of the FPR flat mirror. This third coil was added for extra freedom in generation of non-linear field-gradients while measuring the effect of the Stycast magnetization.

Stycast magnetization and total field.

During the initial stage of the experiment it became clear that the Stycast 1266 had acquired a small diamagnetic magnetization and the meniscus in contact with the top part of the sample tube was enough to create substantial inhomogeneity in the magnetic field inside the sample volume. The Stycast magnetization creates a cylindrically symmetric local field with a maximum at the sample volume wall.

This was not totally unexpected, as similar behaviour has been previously observed in Stycast cooled to liquid helium temperature. In our case the magnetization turned out to be much stronger though, which is in agreement with the temperature being lower.

In order to estimate the strength of the magnetization the difference in the magnetic field magnitude between the top of the sample volume and the local maximum next to the Stycast wall was measured from the spectra with varying known field gradients. The gradients were created with both the radiation shield anti-Helmholtz coils and the parabolic gradient coil located directly above the flat mirror of the FPR cavity.

These differences were then compared to simulations run with corresponding currents and varying values for the magnetization.

In the simulations all gradient coils and the Stycast sample container were modelled in detail, according to the experimental setup. This computationally challenging scenario including large structures but still demanding high local accuracy was feasible because a FEM software, FlexPDE, with variable and locally adjustable mesh spacing, was used.

The simulations were run in a cylindrically symmetric 2D mesh, because all the relevant details followed that symmetry. The differential equation being integrated was

$$\boldsymbol{\nabla} \times \left(\frac{(\boldsymbol{\nabla} \times \mathbf{A}) - \mathbf{M}}{4\pi} \right) + J_{parab} + J_{AH} = 0 \qquad (3.7)$$

where the magnetic vector potential $\mathbf{A}$ is the variable. Other parameters are magnetization $\mathbf{M}$ and the current densities J_{parab} and J_{AH} in the parabolic and anti-Helmholtz coils, correspondingly. In this symmetric case $\mathbf{A}$, J_{parab} and J_{AH} are all perpendicular to the computational mesh plane.

Due to the relation $\mathbf{B} = \boldsymbol{\nabla} \times \mathbf{A}$, in cylindrical coordinates it follows that the radial and axial components of $\mathbf{B}$ are

$$B_r = \frac{\partial \mathbf{A}}{\partial z} \tag{3.8}$$

$$B_z = -\frac{1}{r}\frac{\partial (r\mathbf{A})}{\partial r} \tag{3.9}$$

An overall match between the measured and simulated fields for a range of different gradient coil currents was found with a Stycast magnetization of $\mathbf{M} = -0.8$ G.

In figure 3.6 two examples of calculated $\mathbf{B}$ field configurations are shown. The top graphs show almost the entire computation grid and the two lower graphs show increasing magnifications around the top of the sample volume area.
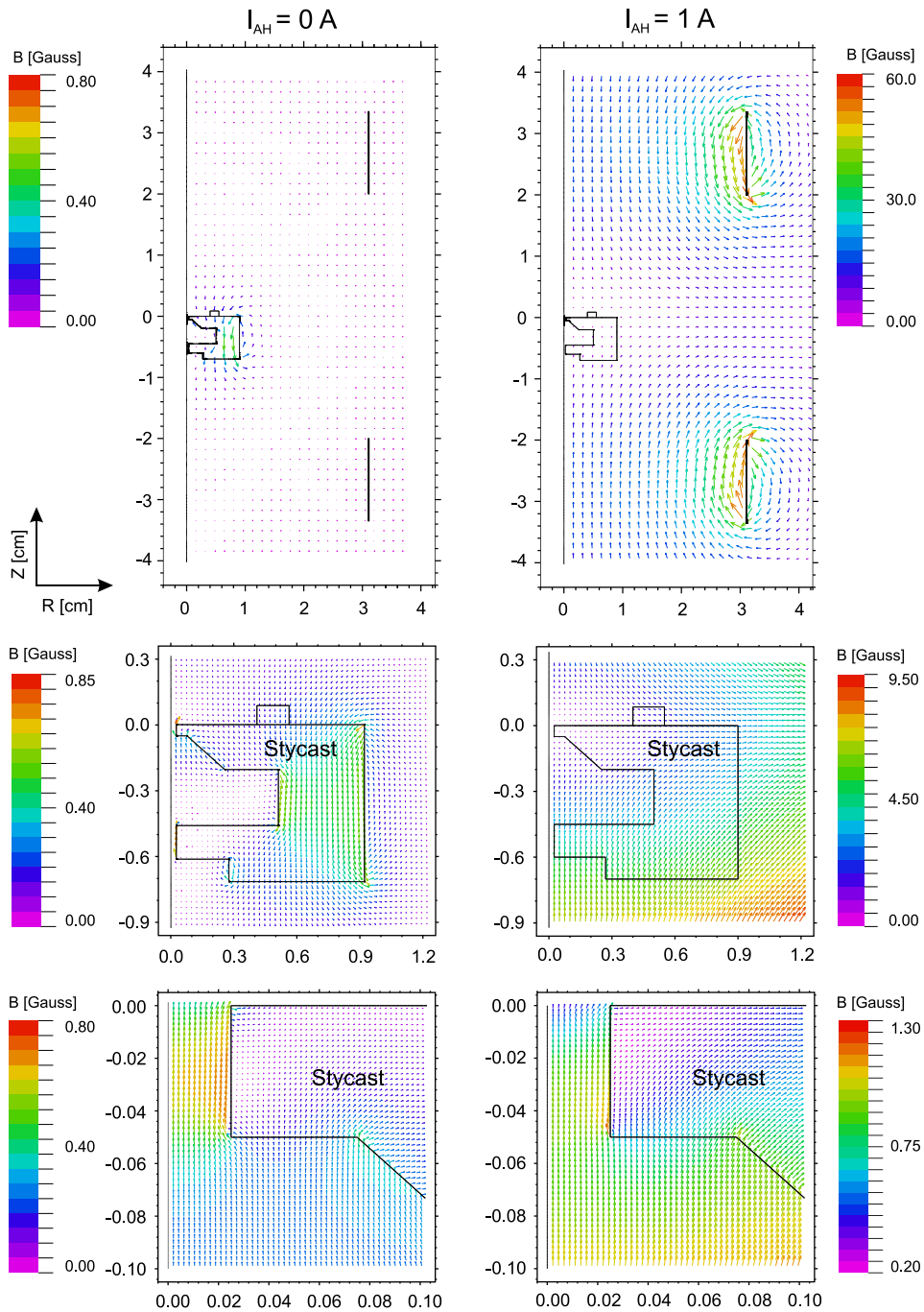
Figure 3.6: Examples of field simulations with anti-Helmholtz coil currents $I_{aH} = 0$ A and $I_{aH} = 1$ A.

3.3 Experimental procedures & results

3.3.1 Recording the spectra

The hydrogen level diagram in high magnetic field is shown in figure 3.7. The ESR spectrometer couples the states a and d, or b and c, depending on the resonance conditions, namely the magnetic field $\mathbf{B}$ and the ESR frequency $f = 2\pi\omega_L$ according to $\omega_L = \gamma_e B$. In these experiments the b-c transition was utilized.

With our ESR spectrometer two different detection methods were used: continuous wave (CW) and pulsed ESR.

Continuous wave ESR

In our setup the CW spectra are measured by scanning the magnetic field through the resonance while keeping the micro wave field frequency stabilised. Historically the recorded spectra have been shown as a function of the (magnetic) sweep field. As it is the total field which defines the resonant condition, the areas inside the sample volume with higher local field come to resonance with smaller sweep field values and are shown on the left hand side of the spectra. The single sweep times for the CW spectra can be adjusted from ≈ 1 s to many tens of seconds.
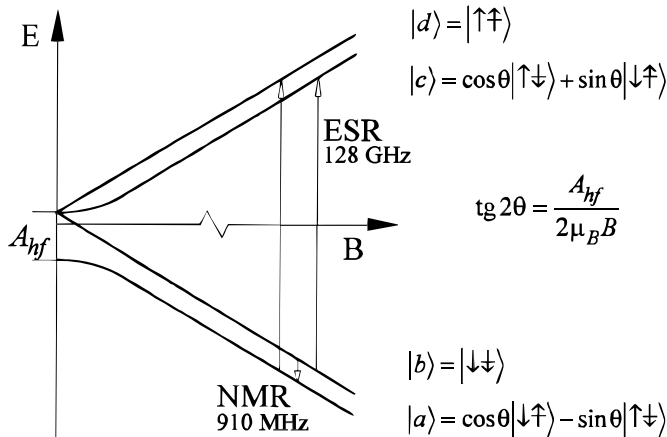

Figure 3.7: The level diagram of hydrogen atom in high magnetic field. The arrows in the state vectors indicate the directions of electron and nuclear spins.

Pulsed ESR

In the pulsed ESR technique, instead of a constant amplitude single frequency microwave, a short pulse with a controllable duration and shape of the amplitude envelope is sent to the resonator. The pulse creates a small transversal magnetization and subsequently the free induction decay (FID) signal is recorded. In the pulsed ESR technique the magnetic field is in fact kept constant during the detection and the frequency distribution during the excitation pulse is the Fourier transform of the temporal distribution of the pulse. Naturally the regions of the sample in higher local field are resulting in higher frequencies. When the spectra recorded with pulsed ESR are shown against a frequency axis with rising values from left to right, the spectra are horizontal mirrors of the corresponding CW spectra.

The possibility of modifying the pulse durations and shapes is an important feature of the pulsed ESR technique, because it renders the possibility of tailored, broadband excitation, with a chosen central frequency. Another benefit of the pulsed excitation compared to the CW ESR is that the detection is separated from the excitation, i.e. the detection is also broadband and not tied to the scan of the resonance. Furthermore, the FID signals contain information about the temporal evolution of the spin dynamics. In practice the FID signals are constructed as an average over many thousands of individual detections. In our experiments the excitation pulses durations range from 0.5 μs to 20 μs with a maximum excitation power of $\approx$ 100 nW. The maximum achievable tipping angle of the spins with our pulses is a few milliradians. The FID signal detection is performed at the intermediate frequency around 100 MHz. We routinely used 1 ns sampling rate with 2^{15}-2^{17} samples per detection. The high speed data collection as well as the averaging is done by the Agilent digitizer. The spectra are then extracted from the FID signals by calculating their Fourier transforms. And as the Fourier transform is complex, a two component spectrum corresponding to both the traditional absorption (symmetric) and dispersion (antisymmetric) signals is received. This computational step provides still other degrees of freedom for the analysis.

In figure 3.8 CW and pulsed ESR spectra and the FID it originated from are shown. The conditions in which these spectra were recorded were similar. The spectra are very similar but some differences are also visible. This emphasizes the fact that both of these recording techniques and especially their combination with the possibility for comparisons between them can be very helpful in understanding the behaviour of the system.
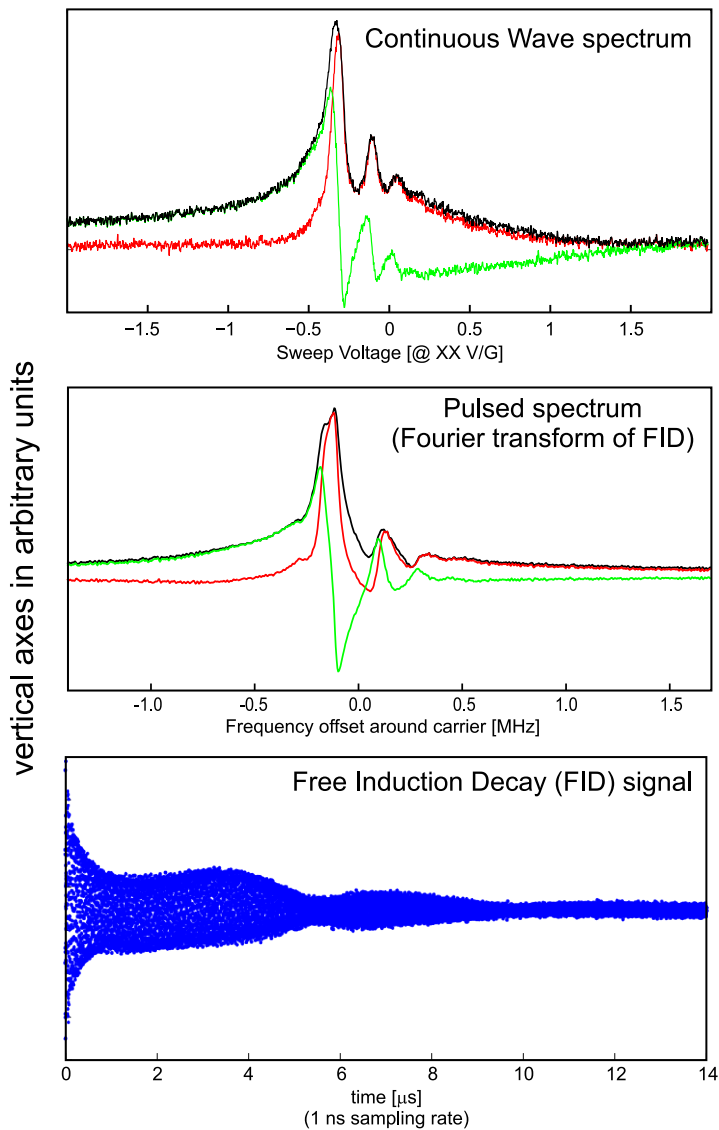
Figure 3.8: Comparison between continuous wave and pulsed spectra. The two upper frames show absorption signals (red lines), dispersion signals (green lines) and their sum of squares (black lines). In the bottom frame the FID signal corresponding to the pulsed spectrum is shown. The phase difference between absorption and dispersion signals is 90 degrees for both detection mechanisms, but the total phase of the detected signal is arbitrary and therefore appropriately chosen during data analysis.

3.3.2 Experiment cycle

The experiment cycle can be divided into five stages:

I **Accumulation**: Each new experiment cycle begins with heating the level meter enough to empty the compression volume of helium in order to open the hydrogen inlet tube. The hold time defines the amount of accumulated hydrogen and thereby affects the final density after compression. The maximum densities accumulated with our hydrogen source were about $5 \cdot 10^{15}$ cm^{-3}.

II **Pre-compression**: Helium is pumped back into the compression/sample volume by ramping down the heating of the level meter. The hydrogen sample is compressed towards the top of the compression volume and into the sample volume. During this ramp the helium level in the level meter drops from the reservoir volume down to the high sensitivity region, which can be seen as a sharp edge in the frequency response.

III **Pause**: As there are also a-state atoms present in the initially accumulated sample, a pause in the compression is needed for letting them recombine before reaching high densities. Otherwise the recombination heat can lead to a runaway recombination of the whole sample.

IV **Final Compression**: After depletion of the a-state atoms the final compression of the doubly polarized sample is conducted. For reaching the highest densities a two stage ramp of the level meter heating is used, reducing the speed of compression towards the end.

V **Sample decay**: After reaching a desired level of compression the heating of the level meter is stabilized and the decay of the sample begins. During the decay the hydrogen pressure, and therefore volume, inside the sample volume decreases affecting the level of helium in the other volumes, including the level meter. Knowing the geometry of the setup the height of the sample can be accurately calculated from this decay induced frequency change. The height of the sample is the distance between the top of the sample volume and the surface of the compressing helium. Also, knowing the liquid helium density, the density of the hydrogen sample can be calculated, as explained in reference [150].
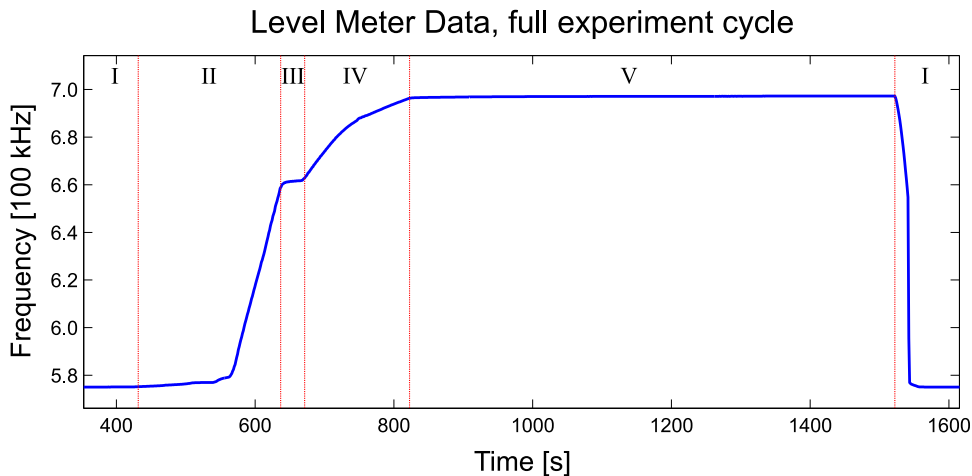
Figure 3.9: Level meter data of one full experiment cycle. Different stages of the cycle are marked with roman numerals and separated by red vertical lines.

3.3.3 Final compression and sample decay

The most important stages during the experiment cycle regarding the results of the experiment are the stages IV and V. The final level meter heating value down to which it is ramped mostly defines the peak density and residual height (geometry) of the sample. As well as leaving the compression to a very low value, such that the helium level does not even reach the Kapton tube (sample volume), the sample can also be over-compressed, so that after the hydrogen density has decayed to zero the sample volume is filled with helium. During these over-compressing experiment cycles the sample usually evolves into a bubble at the top of the sample volume, fully immersed in the compressing liquid helium. In figure 3.10 schematics of three different compression schemes are shown with the corresponding level meter data.

Determining sample height and density

The height and density of the samples can only be accurately determined for compressions with a final heating value with which the helium reaches the sample volume but does not fully fill it after the hydrogen density has decayed to zero (compression **b** in figure 3.10).

During the decay of the sample, when the level meter heating and there-
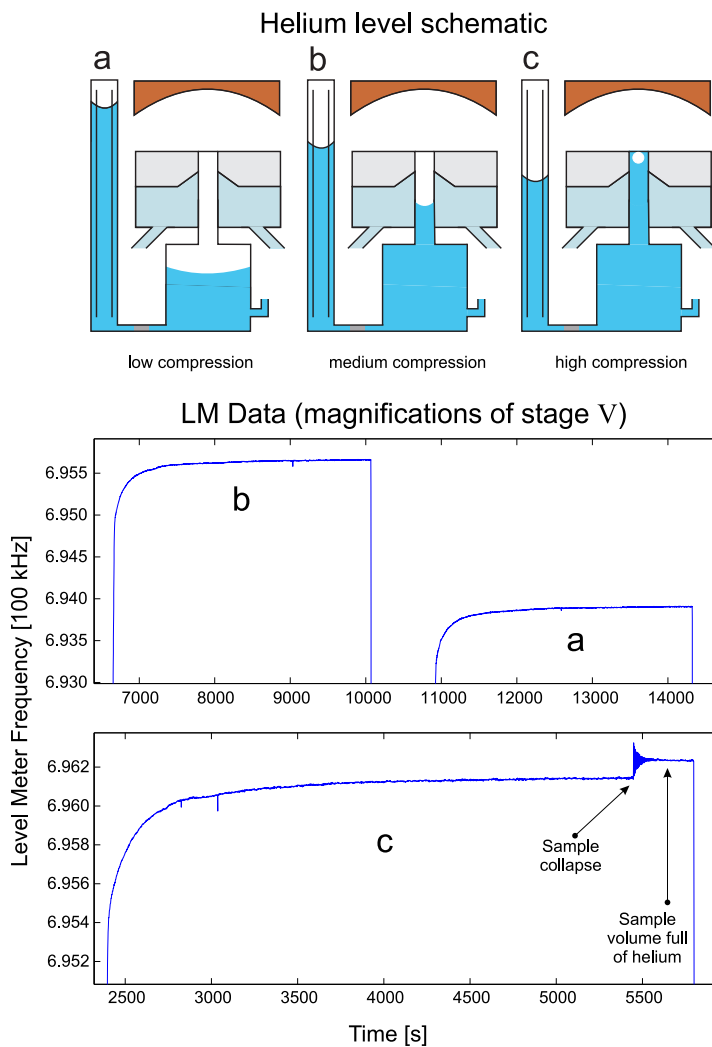
Figure 3.10: Three different compressions. a) Low-density compression ending before helium enters the Kapton tube. b) Medium-density compression: compression helium enters Kapton tube. This leads to higher densities and well defined sample volume geometry. Varying heights can be achieved. c) High-density compression: due to high pressure of compression helium the hydrogen gas evolves into a bubble before collapsing.

fore temperature difference ΔT between level meter and sample volumes is kept constant, the density of the sample corresponding to a specific spectrum can be calculated from the helium level height difference; it is simply

the density corresponding to a pressure matching the hydrostatic pressure of liquid helium for the given height difference. The height change of the helium again follows directly from the geometry of the helium volumes and the difference between the level meter frequency values between zero and non-zero hydrogen densities. For defining the geometry the cross-sections of all the volumes into which the helium rises have to be known. In order to have an accurate zero density frequency reading it is crucial that helium does not fill the sample volume at the end of the decay. The feasible density range in our experiments is from $\approx 1 \cdot 10^{15}$ up to an estimated $5 \cdot 10^{18}$ atoms/cm^3. These highest densities are reached in the bubbles for which there is no accurate density data. The highest reliably determined densities were $\approx 2 \cdot 10^{18}$ cm^{-3}.

The densities extracted from the level meter data were compared to estimates based on calorimetric measurements (recombination heat) and ESR absorption data. Accurate calorimetric measurements could only be carried out before filling the liquid helium coolant volume, because the heat dissipated directly to the mixing chamber through helium could not be measured.

In order to determine the height of the sample also the level meter frequency value corresponding to a liquid helium filled sample volume has
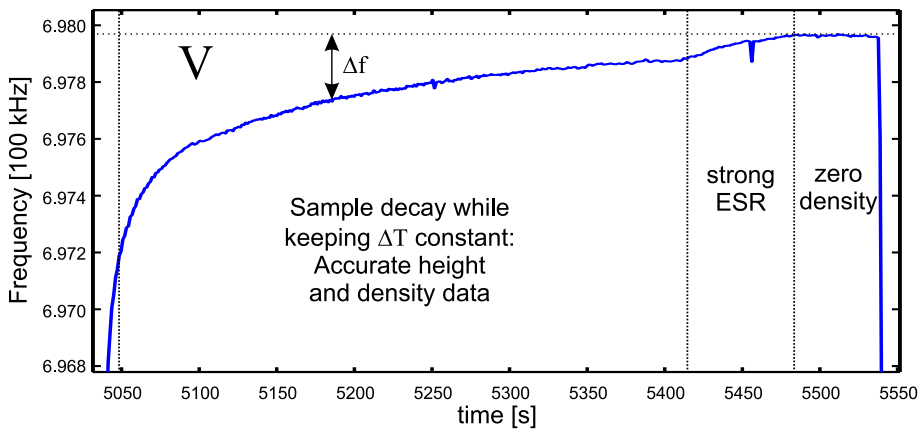

Figure 3.11: Stage V level meter data for a compression ending with zero hydrogen density in a non-helium-filled sample volume. The hydrogen sample is deliberately desroyed by strong ESR excitation inducing recombination. In the end we get an empty space in the compression region, which is used as a reference of the zero density level.

to be known. This can be measured by ramping the level meter heating down enough to fill the sample volume with helium. After the sample volume is full of helium, the heating has to be ramped back to a desired steady-state heating value for the frequency measurement, as the (full and zero density) frequencies are specific to the level meter heating. Once the sample volume is filled with helium, as it is sealed from the top, it will only be emptied after strong heating of the level meter. This usually requires a heating strong enough to open the hydrogen valve. Comparing the helium filled and spectrum specific frequencies the heights of the samples can be calculated, again based on the geometry of the liquid helium volume.

3.3.4   Data analysis

Altogether there are four different variables against which we have compared the behaviour of the spin wave modulations:

- Magnetic field gradient
- Hydrogen density
- Sample geometry (height of the cylinder)
- Temperature

The type of the magnetic field gradient had the strongest influence on the position, spacing, and behaviour of the modulations, defining the basic structure of the spectra. Depending on the type of the gradient these basic structures had different responses to variations in the other parameters. Therefore we first categorized the spectra according to the types of the magnetic field gradients. The four different types of gradient are as follows:

- **Large negative gradient**, for which the magnetic field magnitude increases downwards, away from the rf excitation region at the top the sample volume.

- **Natural gradient**, which is the magnetic field profile without any influence of the external coils. This gradient has a reasonably strong field maximum next to the sample volume wall due to the magnetized Stycast meniscus.

- **Optimized homogeneity**, for which the changes in magnetic magnitude have been minimized in the uppermost part of the sample volume.

- **Large positive gradient**, for which the magnetic field magnitude decreases downwards. This is the opposite to the large negative gradient.

In figures 3.12 and 3.13 these four types of gradient are shown next to representative spectra. In each of the panels multiple consecutive spectra from one experiment cycle are shown. Therefore, in each panel the influence of the decay of the hydrogen sample is also visible, the first spectrum with highest density/longest sample geometry being on the top while the last spectrum with lowest density and shortest sample height is the bottom one.

While the sample decays during the stage of constant level meter heating both density and height change simultaneously. Using the level meter data both of these parameters can be extracted, but for a differing height/density combination another experiment cycle has to be performed with a different hydrogen sample accumulation time or compression curve, or both.

Spectra in large negative gradient

These spectra had multiple strong and well separated peaks on the local high field side of the spectra. The modulation peak positions had a $n^{-1/3}$ density dependence and their inter-peak distances scaled as the distances between the maxima of Airy functions, which are the solutions of a differential equation like equation 3.22, with a linear "potential" term; in this case the term $\gamma_e \delta H_0$. The temperature dependence of these modulations was very weak, but detectable. The inter-peak distances were slightly increased at higher temperatures.

Spectra in natural gradient

The spectra in the natural gradient, or more accurately any gradient with a reasonable local field maximum outside the strongest rf field excitation area, had a double peak structure. It was recognized that the second peak always appeared on the high local field side of the main ESR absorption peak (on the left of the main peak in CW spectra). Also, comparing the data with the magnetic field simulations it was found that the separation between these two peaks matched the calculated magnetic field difference between the ESR excitation area and the local field maximum. In quantifying the source of the second peak it was of great help that we had data from the two previous experimental cells, which had different magnetic characteristics.
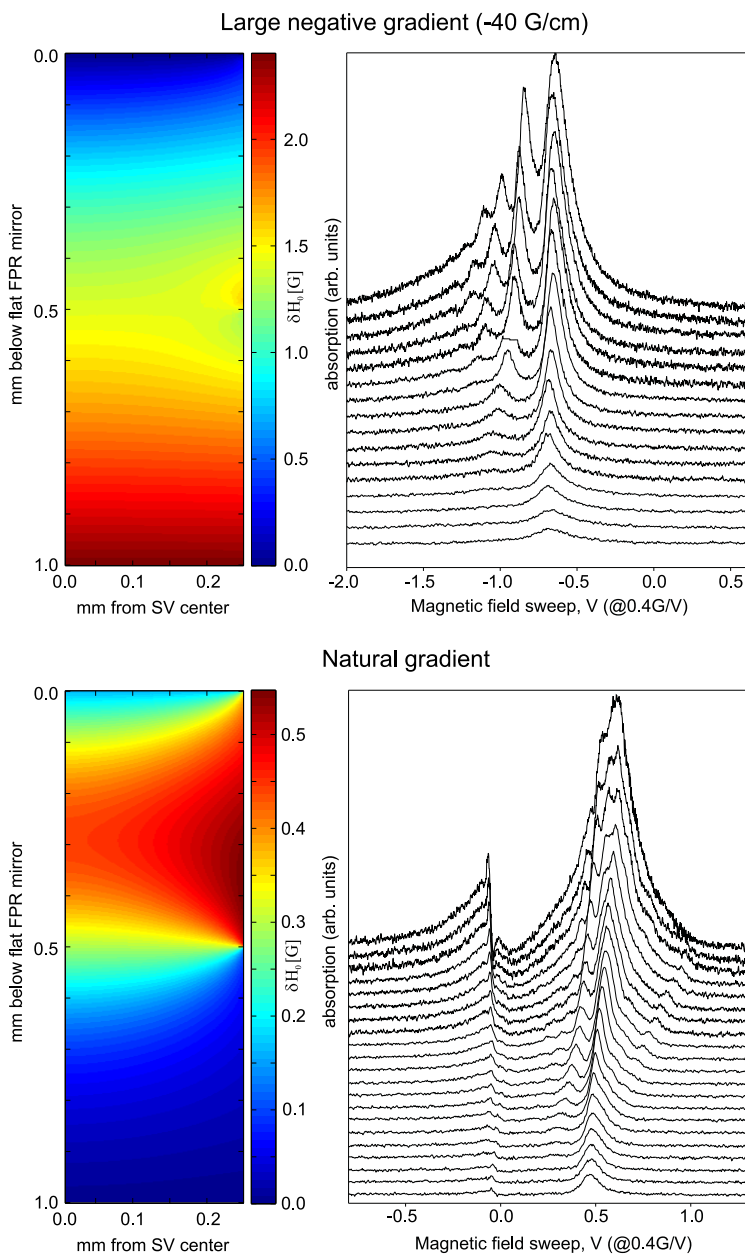
Figure 3.12: The magnetic field profiles and corresponding spectra for large negative gradient and natural gradient. The horizontal axis follows the tradition of CW ESR and it is a mirror image of what is presented in **paper V**.
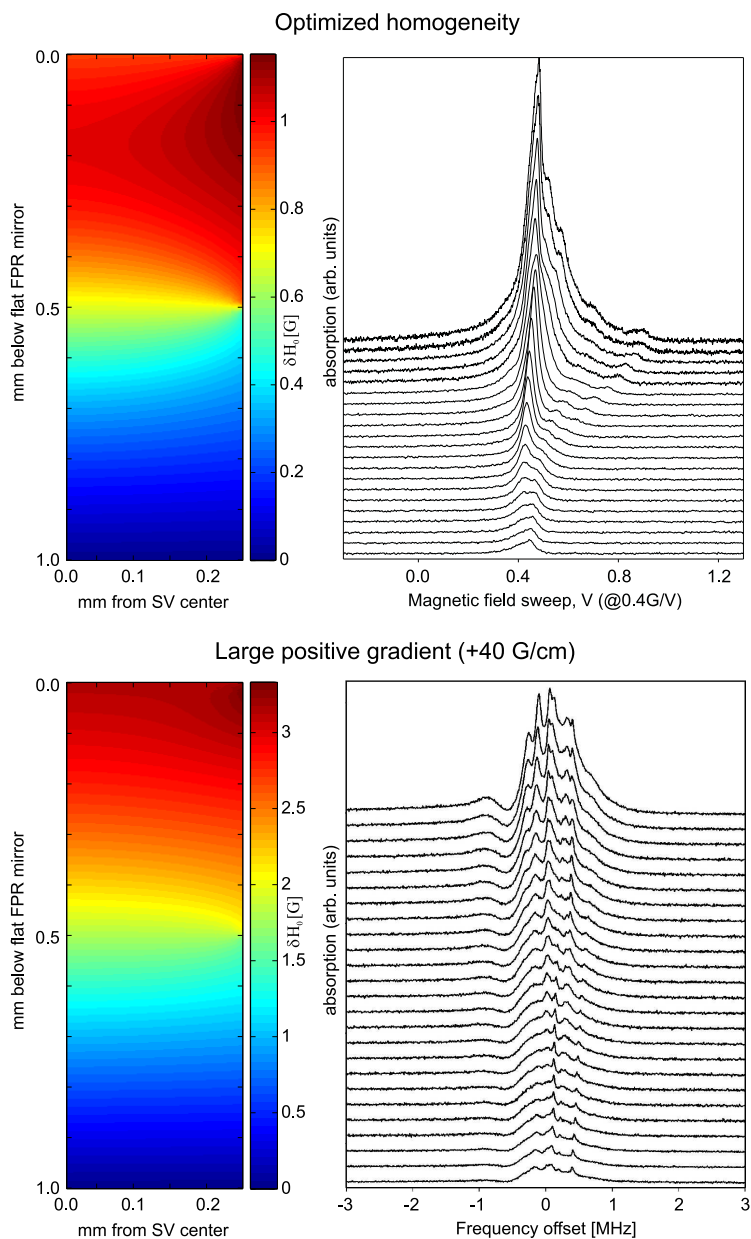
Figure 3.13: The magnetic field profiles and corresponding spectra for optimized homogeneity and large positive gradient. In the upper frame the horizontal axis follows the tradition of CW ESR. The lower frame spetra are recorded with pulsed ESR instead.

Spectra in optimized homogeneity

The modulations in the spectra recorded with optimized field homogeneity are discreet compared to modulations in the spectra in other types of gradients. The distinct features in this type of spectra are the low contrast peaks on the lower local field side of the main peak, with a clear hydrogen sample height dependence. These are the only modulations for which we have a confirmed geometry dependence.

Spectra in large positive gradient

The spectra in large positive gradient have a large number of closely separated modulation peaks. As with the spectra in optimized homogeneity, the origin of these modulations is still uncertain.

3.3.5   Spin wave simulations

Magnetostatic modes

Following Walker's derivation in [95], we get a wave equation for the magnetostatic spin waves. The magnetostatic approximation requires that

$$\boldsymbol{\nabla} \times \mathbf{H} = 0 \tag{3.10}$$
$$\boldsymbol{\nabla} \cdot \mathbf{B} = 0 \tag{3.11}$$

with the relation that $\mathbf{H} = \mathbf{B} - 4\pi\mathbf{M}$, where $\mathbf{M}$ is the magnetization. The equation of motion for the magnetization is the Landau-Lifshitz equation

$$\frac{d\mathbf{M}}{dt} = \gamma_e \left(\mathbf{M} \times \mathbf{H} \right). \tag{3.12}$$

We write the magnetic field as a sum of the static field and the oscillating part as

$$\mathbf{H} = \mathbf{H_z} + \mathbf{h}e^{i\omega t} \tag{3.13}$$

and similarly the magnetization as

$$\mathbf{M} = \mathbf{M_z} + \mathbf{m}e^{i\omega t} \tag{3.14}$$

where $\mathbf{M_z}$ is the saturation magnetization and large compared to $\mathbf{m}$, which has only the transversal components m_x and m_y. From (3.10) and (3.11) it follows that for the oscillating parts it is also required that

$$\boldsymbol{\nabla} \times \mathbf{h} = 0 \tag{3.15}$$
$$\boldsymbol{\nabla} \cdot \mathbf{b} = \boldsymbol{\nabla} \cdot (\mathbf{h} + 4\pi\mathbf{m}) = 0. \tag{3.16}$$

Because of the condition stated in equation (3.15), a scalar potential Ψ can be introduced, for which

$$\mathbf{h} = \nabla\Psi. \tag{3.17}$$

Combining the equations (3.16) and (3.17), and using the linear approximation of (3.12) for finding the relations between the components of $\mathbf{m}$ and Ψ one can find the wave equation

$$\left(\lambda_i \left(\frac{\partial^2}{\partial x^2} + \frac{\partial^2}{\partial y^2} \right) + \frac{\partial^2}{\partial z^2} \right) \Psi_i = 0 \tag{3.18}$$

where, in terms of reference [103]

$$\lambda_i = \frac{H_z B_z - (\omega_i/\gamma_e)^2}{H_z^2 - (\omega_i/\gamma_e)^2}. \tag{3.19}$$

In (3.19) $B_z = H_z + 4\pi M_z$, where B_z and H_z are the magnitudes of the corresponding static field components, M_z is the saturation magnetization, γ_e is the electron gyromagnetic ratio and ω_i is the frequency of the magnetostatic mode Ψ_i.

In the simulations solutions for equation (3.18) were searched numerically. As with the magnetic field simulations, the straightforward scripting and the built-in eigenvalue algorithms of FlexPDE allowed running simulations with various symmetries (1D axial, 1D and 2D cylindrically symmetric, eq. (3.21), and full 3D without assumptions about symmetries, eq. (3.19)) with minimal changes in the scripts. 3D simulations also allowed testing various geometries by changing the height of the sample volume, including simulations with a hemispherical bottom of the sample cell, mimicking the liquid helium meniscus at the lower end of the sample volume.

The cylindrical symmetry of the sample volume naturally implied that the solutions should be of the form, again in terms of [103]:

$$\Psi = \psi(r)e^{-i(\beta z + m\phi)} \tag{3.20}$$

where $\psi(r)$ has to satisfy the equation

$$\left(\lambda_i \left(\frac{\partial^2}{\partial r^2} + \frac{1}{r}\frac{\partial}{\partial r} - \frac{m^2}{r^2} \right) - \beta^2 \right) \psi_i(r) = 0. \tag{3.21}$$

In (3.20) and (3.21) $m \in \mathbb{Z}$ is the azimuthal mode number and $\beta \in \mathbb{R}$ is the propagation constant in axial direction. As shown in [103], the eigenfrequencies ω_i can be labeled with indices (ζ, m, r), where $\zeta = |\beta|R$ and

$R = 0.25$ mm is the radius of the sample volume. In the simulations, assuming cylindrical symmetry, β and m were varied manually and simulations were run for multiple combinations.

Due to the facts that $\nabla^2 \Psi = 0$ outside the hydrogen volume and that Ψ must vanish at infinity, the boundary conditions in the simulations were set by forcing the conditions $\lambda_i = 1$ outside the sample volume, and $\Psi = 0$ at the outer boundary of the simulation mesh. In most of the simulations the outer boundary was set to $3R$ in radial direction and to a similar distance in the axial orientation. At the boundary between the sample volume and the external computation mesh it was required that Ψ_i is continuous.

Despite a multitude of various simulated scenarios, no match was found between the simulations of magnetostatic modes and the experimentally observed modulation patterns.

ISRE spin waves

Since our experiments are conducted in high magnetic field, the conditions $S_+ \ll S$ and $S_z \approx S \approx 1$ are met. Furthermore, if $\mu \gg 1$ equation (3.5) can be simplified to

$$\frac{\partial S_+}{\partial t} = D_0 \frac{\epsilon}{\mu} \nabla^2 S_+ + \gamma \delta H_0 S_+. \tag{3.22}$$

In the simulations eigenmodes and corresponding eigenfrequencies were numerically searched for equation (3.22). For D_0 the value $5 \cdot 10^{18}/n$ was used, where n is the density. 1D simulations with $\mu \approx -8$ and a linear gradient of -40 G/cm produced eigenmodes with peak separations matching the ones measured from spectra in large negative gradient. This was interpreted as a further confirmation of ISRE as the origin of these modes.

Using these same parameter values eigenmode simulations in 3D were run for the assumed magnetically trapped ISRE spin wave modes, using the calculated magnetic field profiles as δH_0. A large number of trapped eigenmodes was found. In figure 3.14 examples of a few low-excitation modes are shown corresponding to the magnetic field profile of the natural field gradient. In figure 3.15 the calculated eigenmode separations are compared to a measured spectrum, positioned to the estimated local field maximum. The mode separations are very small compared to the structures in the measured spectrum.

3.3.6 Summary

Of the four differently behaving modulation patterns observed in the spectra two were clearly identified as following the behaviour expected from ISRE induced electronic spin waves.

In large negative gradient the spatial separation and density dependence of the modulations matched the spatial separation of the amplitude maxima of solutions of equation (3.22) in a linear gradient. The solutions of this kind of a wave equation in a linear gradient are known as Airy functions.

The other identified magnetic field dependent modulation in the spectra was the trapped spin waves, again following the behaviour expected from a phenomenon whose time evolution follows equation (3.22). These two clear
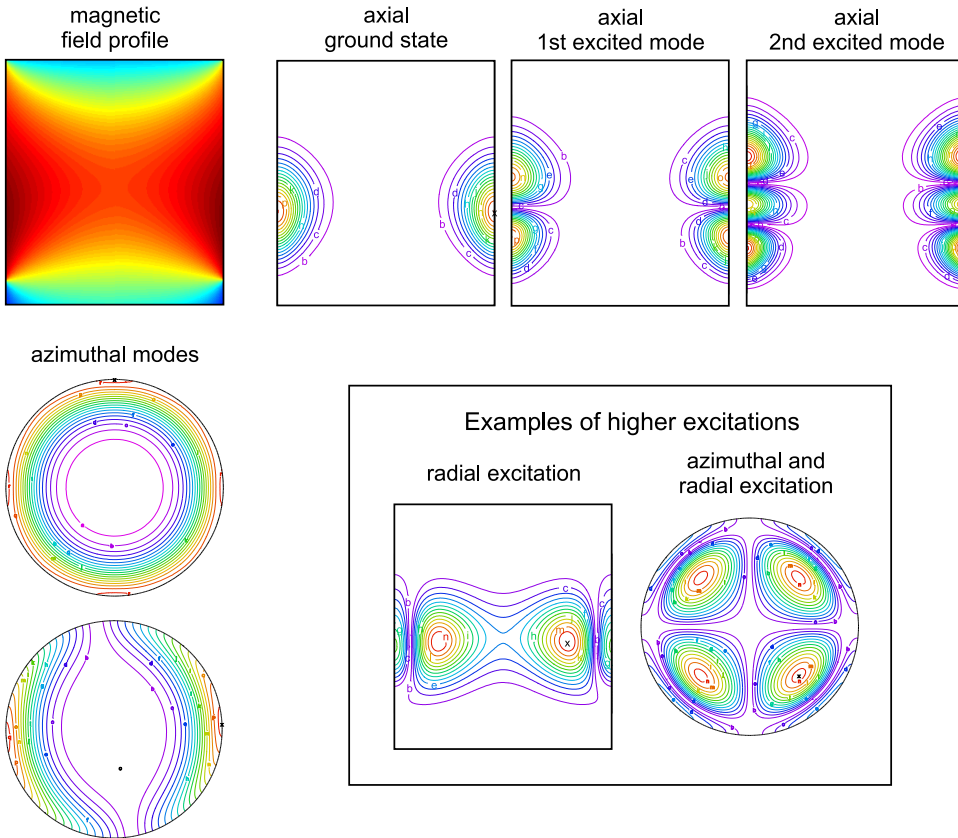

Figure 3.14: Examples of calculated eigenmodes in the local field maximum next to the wall of the sample volume. The field profile is of the natural gradient type.
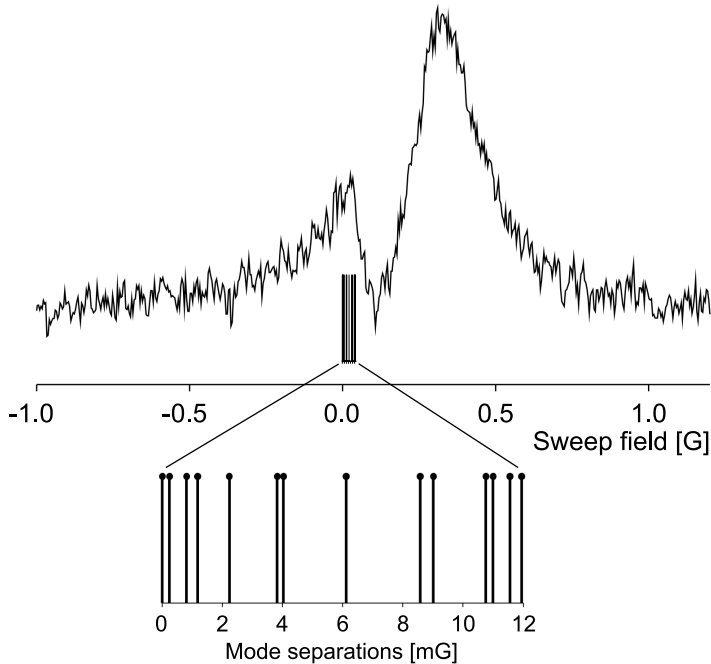
Figure 3.15: Simulated mode separations of magetically trapped ISRE spin wave modes compared to recorded spectrum in natural gradient magnetic field.

cases were reported in **paper V**.

On the other hand, there were two types of magnetic field gradients in which the modulations in the recorded spectra were not clearly identified. It is possible that some of these modulations are explained by the ISRE induced spin waves, especially the kind of modulations seen in the large positive gradient. These might well be modes trapped between the top of the sample volume and a steeply rising magnetic field induced potential.

The modes with a sample height dependency seen in magnetic fields with optimized homogeneity bear some characteristics of magnetostatic waves, but their inter-peak separation is too large to be explained with the simple theory assuming homogeneous external magnetic field. Some of the new computational techniques might allow taking into account the magnetic field variations and be helpful in the analysis.

3.3.7 Future

In addition to trying to understand the behaviour of the modulations of the spectra in all available magnetic field gradients in cylindrical shapes of various lengths, the special geometry of a spherical sample available during the last seconds of strong compression deserves attention. For these measurements it would also be beneficial if one could control the level meter heating accurately enough, or through an automatic feedback stabilize the hydrogen bubble against implosion due to increasing liquid helium surface tension.

Another very interesting subject for further studies is the narrow, large amplitude feature observed within the trapped ISRE spin wave peak, shown in figure 3.16. The FID signal of this spectrum has a long constant frequency tail resembling the FID signals reported in references [145, 146] and interpreted as a homogeneously precessing domain (HPD), or a BEC of magnons. Curiously the total phase adjustment of the detected signal resulting in traditional absorption and dispersion components for the broad background spectrum is different from the phase adjustment needed for achieving this with the offset FID signal of narrow component only. This phase difference varied between 90° and 180° depending on the experimental conditions. The magnetic field gradient for the spectrum shown in figure 3.16 is between the previously described natural and optimized homogeneity gradients. It has a local field maximum close to the top of the sample volume.

Also, a more detailed study of the spin transport phenomenon and especially a more careful measurement of the parameters D_0 and μ would be important. For these the customizable rf excitation pulse profiles might prove to be useful.

For all these new measurements a better control of the magnetic field is needed. Rather than creating the local field maxima with a static magnetization of the Stycast, a controllable set of coils should be used.
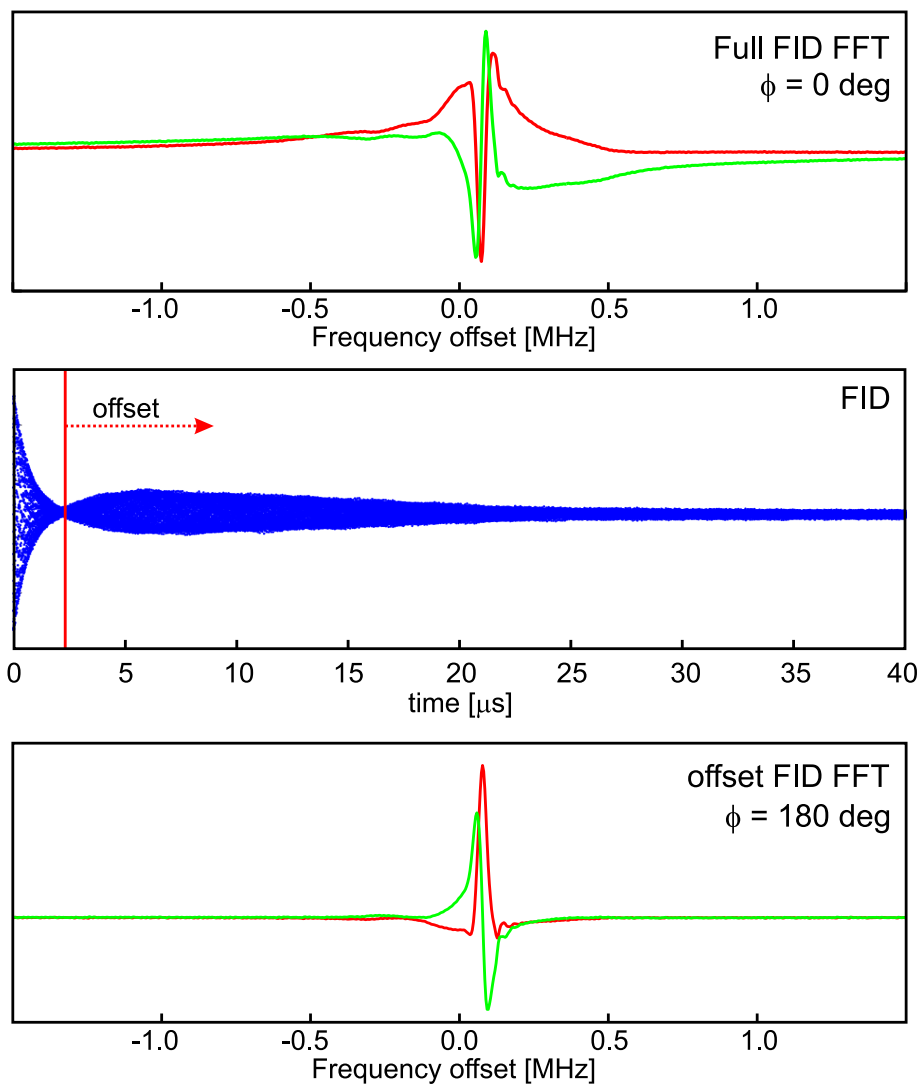
Figure 3.16: Possible observation of homogeneously precessing domain in atomic hydrogen. The red (absorption) and green (dispersion) curves are the two components of the Fourier transform. Upper frame: Fourier transform of the full FID signal. Center frame: FID. Lowest frame: Fourier transform of the FID with an offset. The first 2.3 μs of the FID signal have been left out of the Fourier transform taking into account only the long living signal of the narrow feature which coincides with the position of the magnetic field maximum. In the figure the values of the total phase adjustment ϕ are also shown. The red (absorption) and green (dispersion) curves are the two components of the Fourier transform. Upper frame: Fourier transform of the full FID signal.

Chapter 4

Conclusions

In the research presented in this thesis the different spin-states of atoms and electrons have served both as the tools for manipulating the dynamics of the cold gaseous sample and as the research subject in themselves. In the Bose-Einstein condensate experiments with ^{87}Rb the different magnetic sub-states defined by the spin-orientations allow, in conjunction with magnetic field gradients and resonant rf fields, controlled trapping and releasing of the sample atoms. Instead, in the experiments with atomic hydrogen dynamics it was the dynamics of the spin-states which was the main subject of the study.

In **paper I** it was shown that the frequency and phase of the matter wave interference pattern originating from a Bose-Einstein condensate using two frequency separated rf fields follows the frequency and phase separation of the outcoupling field. This result shows that also the dynamics of the rf field has to be taken into account in the interpretation of possibly more complex future experiments.

In **paper II** a theoretical model for the outcoupling scenario described in **paper I** was introduced. The model is based on a wave-packets consisting of continuous loading of a continous spectrum of atomic eigenstates in the given potential. An important consequence of this continuity is the localization of the resulting wave-packet, in contrast to the unphysical infinite wave-functions of individual Airy-functions. The wave-packet model also correctly reproduced the behaviour of the fringe visibility due to unequal outcoupling rf fields.

The perturbations in the spectra recorded for the studies presented in **paper IV** complicated the analysis of some of the previously executed clock-shift measurements and deserved further clarification. During the analysis of the new experimental data recorded with a new purpose-built

experimental setup, the construction of which is described in this thesis, it became clear that a majority of these perturbations was induced by electronic identical spin rotation effect (ISRE) spin waves. Nuclear spin waves of this type have been reported before, but in **paper V** we reported for the first time an observation of electronic ISRE spin waves. It was also confirmed that, in addition to modes confined solely by material walls of the experimental chamber, these modes can be trapped in a combination of material walls and a local magnetic field maximum. The experimental verification of the long time ago predicted electronic spin waves is an significant result as it provides the basis for a whole set of new spin-interaction experiments, including e.g. a careful study of spin diffusion coefficient and a more detailed and better controlled measurement of the assumed observation of interlocked spin-precession, a homogeneously precessing domain.

Bibliography

[1] M. H. Anderson, J. R. Ensher, M. R. Matthews, C. E. Wieman, and E. A. Cornell. Observation of Bose-Einstein condensation in a dilute atomic vapor. *Science*, 269:198, 1995.

[2] K. B. Davis, M.-O. Mewes, M. R. Andrews, N. J. van Druten, D. S. Durfee, D. M. Kurn, and W. Ketterle. Bose-Einstein condensation in a gas of sodium atoms. *Physical Review Letters*, 75:3969, 1995.

[3] C. C. Bradley, C. A. Sackett, J. J. Tollett, and R. G. Hulet. Evidence of Bose-Einstein condensation in an atomic gas with attractive interactions. *Physical Review Letters*, 75:1687, 1995.

[4] A. Einstein. Quantentheorie des einatomigen idealen gases. *Sitzungsber. Kgl. Preuss. Akad. Wiss.*, 261, 1924.

[5] A. Einstein. Quantentheorie des einatomigen idealen gases. *Sitzungsber. Kgl. Preuss. Akad. Wiss.*, 3, 1925.

[6] S. N. Bose. Plancks gesetz und lichtquantenhypothese. *Zeitschrift für Physik A Hadrons and Nuclei*, 26:178, 1924.

[7] M. R. Andrews, C. G. Townsend, H.-J. Miesner, D. S. Durfee, D. M. Kurn, and W. Ketterle. Observation of interference between two Bose condensates. *Science*, 275:637, 1997.

[8] D. S. Hall, M. R. Matthews, C. E. Wieman, and E. A. Cornell. Measurements of relative phase in two-component Bose-Einstein condensates. *Physical Review Letters*, 81:1543, 1998.

[9] M. Naraschewski, H. Wallis, A. Schenzle, J. I. Cirac, and P. Zoller. Interference of Bose condensates. *Physical Review A*, 54:2185, 1996.

[10] A. Röhrl, M. Naraschewski, A. Schenzle, and H. Wallis. Transition from phase locking to the interference of independent Bose condensates: Theory versus experiment. *Physical Review Letters*, 78:4143, 1997.

[11] L. de Broglie. *Ann. Phys.*, 3:22, 1925.

[12] C. Davisson and L. H. Germer. Diffraction of electrons by a crystal of nickel. *Physical Review*, 30:705, 1927.

[13] R. J. C. Spreeuw, T. Pfau, U. Janicke, and M. Wilkens. Laser-like scheme for atomic-matter waves. *Europhysics Letters*, 32:469, 1995.

[14] Howard Wiseman, Ana Martins, and Daniel Walls. An atom laser based on evaporative cooling. *Quantum and Semiclassical Optics*, 8:737, 1996.

[15] M. Holland, K. Burnett, C. Gardiner, J. I. Cirac, and P. Zoller. Theory of an atom laser. *Physical Review A*, 54:R1757, 1996.

[16] M.-O. Mewes, M. R. Andrews, D. M. Kurn, D. S. Durfee, C. G. Townsend, and W. Ketterle. Output coupler for Bose-Einstein condensed atoms. *Physical Review Letters*, 78:582, 1997.

[17] H. Steck, M. Naraschewski, and H. Wallis. Output of a pulsed atom laser. *Physical Review Letters*, 80:1, 1998.

[18] E. W. Hagley, L. Deng, M. Kozuma, J. Wen, S. L. Helmerson, K. Rolston, and W. D. Phillips. A well-collimated quasi-continuous atom laser. *Science*, 283:1706, 1999.

[19] R. J. Ballagh, K. Burnett, and T. F. Scott. Theory of an output coupler for Bose-Einstein condensed atoms. *Physical Review Letters*, 78:1607, 1997.

[20] Weiping Zhang and D. F. Walls. Gravitational and collective effects in an output coupler for a Bose-Einstein condensate in an atomic trap. *Physical Review A*, 57:1248, 1998.

[21] M. Naraschewski, A. Schenzle, and H. Wallis. Phase diffusion and the output properties of a cw atom-laser. *Physical Review A*, 56:603, 1997.

[22] Robert Graham and Dan F. Walls. Theory of strong outcoupling from Bose-Einstein condensates. *Physical Review A*, 60:1429, 1999.

[23] Y. Castin, R. Dum, E. Mandonnet, A. Minguzzi, and I. Carusotto. Coherence properties of a continuous atom laser. *Journal of Modern Optics*, 47:2671, 2000.

[24] Immanuel Bloch, Theodor W. Hänsch, and Tilman Esslinger. Atom laser with a cw output coupler. *Physical Review Letters*, 82:3008, 1999.

[25] I. Bloch, T. W. Hänsch, and T. Esslinger. Measurement of the spatial coherence of a trapped Bose gas at the phase transition. *Nature*, 403:166, 2000.

[26] Jens Schneider and Axel Schenzle. Investigations of a two-mode atom-laser model. *Physical Review A*, 61:053611, 2000.

[27] Immanuel Bloch, Michael Köhl, Markus Greiner, Theodor W. Hänsch, and T ilman Esslinger. Optics with an atom laser beam. *Physical Review Letters*, 87:030401, 2001.

[28] Michael Köhl, Theodor W. Hänsch, and Tilman Esslinger. Measuring the temporal coherence of an atom laser beam. *Physical Review Letters*, 87:160404, 2001.

[29] Giovanni Cennini, Gunnar Ritt, Carsten Geckeler, and Martin Weitz. All-optical realization of an atom laser. *Physical Review Letters*, 91:240408, 2003.

[30] Anton Öttl, Stephan Ritter, Michael Köhl, and Tilman Esslinger. Correlations and counting statistics of an atom laser. *Physical Review Letters*, 95:090404, 2005.

[31] T. Donner, S. Ritter, T. Bourdel, A. Öttl, M. Köhl, and T. Esslinger. Critical behavior of a trapped interacting Bose gas. *Science*, 315:1556, 2007.

[32] Giovanni Cennini, Carsten Geckeler, Gunnar Ritt, and Martin Weitz. Interference of an array of atom lasers. *Physical Review A*, 77:013613, 2008.

[33] Nicholas P. Robins, Cristina Figl, Matthew Jeppesen, Graham R. Dennis, and John D. Close. A pumped atom laser. *Nature Physics*, 4:731, 2008.

[34] D. Döring, N. P. Robins, C. Figl, and J. D. Close. Probing a Bose-Einstein condensate with an atom laser. *Optics Express*, 16:13893, 2008.

[35] E. L. Raab, M. Prentiss, Alex Cable, Steven Chu, and D. E. Pritchard. Trapping of neutral sodium atoms with radiation pressure. *Physical Review Letters*, 59:2631, 1987.

[36] J. D. Weinstein and K. G. Libbrecht. Microscopic magnetic traps for neutral atoms. *Physical Review A*, 52:4004, 1995.

[37] J. Reichel, W. Hänsel, and T. W. Hänsch. Atomic micromanipulation with magnetic surface traps. *Physical Review Letters*, 83:3398, 1999.

[38] Dirk Müller, Dana Z. Anderson, Randal J. Grow, Peter D. D. Schwindt, and Eric A. Cornell. Guiding neutral atoms around curves with lithographically patterned current-carrying wires. *Physical Review Letters*, 83:5194, 1999.

[39] Ron Folman, Peter Krüger, Donatella Cassettari, Björn Hessmo, Thomas Maier, and Jörg Schmiedmayer. Controlling cold atoms using nanofabricated surfaces: Atom chips. *Physical Review Letters*, 84:4749, 2000.

[40] N. H. Dekker, C. S. Lee, V. Lorent, J. H. Thywissen, S. P. Smith, M. Drndić, R. M. Westervelt, and M. Prentiss. Guiding neutral atoms on a chip. *Physical Review Letters*, 84:1124, 2000.

[41] Donatella Cassettari, Björn Hessmo, Ron Folman, Thomas Maier, and Jörg Schmiedmayer. Beam splitter for guided atoms. *Physical Review Letters*, 85:5483, 2000.

[42] W. Hänsel, J. Reichel, P. Hommelhoff, and T. W. Hänsch. Magnetic conveyor belt for transporting and merging trapped atom clouds. *Physical Review Letters*, 86:608, 2001.

[43] W. Hänsel, P. Hommelhoff, T. W. Hänsch, and J. Reichel. Bose-Einstein condensation on a microeletric chip. *Nature*, 413:498, 2001.

[44] H. Ott, J. Fortagh, A. Schlotterbeck, A. Grossmann, and C. Zimmermann. Bose-Einstein condensation in a surface microtrap. *Physical Review Letters*, 87:230401, 2001.

[45] Erika Andersson, Tommaso Calarco, Ron Folman, Mauritz Andersson, Björn Hessmo, and Jörg Schmiedmayer. Multimode interferometer for guided matter waves. *Physical Review Letters*, 88:100401, 2002.

[46] A. E. Leanhardt, A. P. Chikkatur, D. Kielpinski, Y. Shin, T. L. Gustavson, W Ketterle, and D. E. Pritchard. Propagation of Bose-Einstein condensates in a magnetic waveguide. *Physical Review Letters*, 89:040401, 2002.

[47] Ron Folman, Peter Krüger, Jörg Schmiedmayer, Johannes Denschlag, and Carsten Henkel. Microscopic atom optics: From wires to an atom chip. *Advances in Atomic, Molecular, and Optical Physics*, 48:263, 2002.

[48] J. Reichel. Microchip traps and Bose-Einstein condensation. *Applied Physics B*, 75:469, 2002.

[49] Jóseph Fortágh and Claus Zimmermann. Magnetic microtraps for ultracold atoms. *Reviews of Modern Physics*, 79:235, 2007.

[50] Jacob Reichel and Vladan Vuletić, editors. *Atom Chips*. WILEY-VCH Verlag GmbH & Co. KGaA, 2011. ISBN 978-3-527-40755-2.

[51] C. Henkel and M. Wilkens. Heating of trapped atoms near thermal surfaces. *Europhysics Letters*, 47:414, 1999.

[52] C. Henkel, S. Pötting, and M. Wilkens. Loss and heating of particles in small and noisy traps. *Applied Physics B*, 69:379, 1999.

[53] C. Henkel, P. Krüger, R. Folman, and J. Schmiedmayer. Fundamental limits for coherent manipulation on atom chips. *Applied Physics B*, 76:173, 2003.

[54] P. K. Rekdal, S. Scheel, P. L. Knight, and E. A. Hinds. Thermal spin flips in atom chips. *Physical Review A*, 70:013811, 2004.

[55] J. Fortágh, H. Ott, S. Kraft, A. Günther, and C. Zimmermann. Surface effects in magnetic microtraps. *Physical Review A*, 66:041604, 2002.

[56] S. Kraft, A. Günther, H. Ott, D. Wharam, and J. Zimmermann, C. Fortágh. Anomalous longitudinal magnetic field near the surface of copper conductors. *Journal of Physics B*, 35:L469, 2002.

[57] M. P. A. Jones, C. J. Vale, D. Sahagun, B. V. Hall, and E. A. Hinds. Spin coupling between cold atoms and the thermal fluctuations of a metal surface. *Physical Review Letters*, 91:080401, 2003.

[58] D. M. Harber, J. M. McGuirk, J. M. Obrecht, and E. A. Cornell. Thermally induced losses in ultra-cold atoms magnetically trapped near room-temperature surfaces. *Journal of Low Temperature Physics*, 133:229, 2003.

[59] J. Estève, C. Aussibal, T. Schumm, C. Figl, D. Mailly, I. Bouchoule, C. I. Westbrook, and A. Aspect. Role of wire imperfections in micromagnetic traps for atoms. *Physical Review A*, 70:043629, 2004.

[60] S. Eriksson, F. Ramirez-Martinez, E. A. Curtis, B. E. Sauer, P. W. Nutter, E. W. Hill, and E. A. Hinds. Micron-sized atom traps made from magneto-optical thin films. *Applied Physics B*, 79:811, 2004.

[61] Philipp Treutlein, Peter Hommelhoff, Tilo Steinmetz, Theodor W. Hänsch, and Jakob Reichel. Coherence in microchip traps. *Physical Review Letters*, 92:203005, 2004.

[62] S. Wildermuth, P. Krüger, C. Becker, M. Brajdic, S. Haupt, A. Kasper, R. Folman, and J. Schmiedmayer. Optimized magneto-optical trap for experiments with ultracold atoms near surfaces. *Physical Review A*, 69:030901, 2004.

[63] S. Groth, P. Krüger, S. Wildermuth, R Folman, T. Fernholz, J. Schmiedmayer, D. Mahalu, and I. Bar-Joseph. Atom chips: Fabrication and thermal properties. *Applied Physics Letters*, 85:2980, 2004.

[64] V. Dikovsky, Y. Japha, C. Henkel, and R. Folman. Reduction of magnetic noise in atom chips by material optimization. *The European Physical Journal D*, 35:87, 2005.

[65] P. Krüger, L. M. Andersson, S. Wildermuth, S. Hofferberth, E. Haller, S. Aigner, S. Groth, I. Bar-Joseph, and J. Schmiedmayer. Potential roughness near lithographically fabricated atom chips. *Physical Review A*, 76:063621, 2007.

[66] T. Nirrengarten, A. Qarry, C. Roux, A. Emmert, G. Nogues, M. Brune, J.-M. Raimond, and S. Haroche. Realization of a superconducting atom chip. *Physical Review Letter*, 97:200405, 2006.

[67] T. Mukai, C. Hufnagel, A. Kasper, T. Meno, A Tsukada, K. Semba, and F. Shimizu. Persistent supercurrent atom chip. *Physical Review Letters*, 98:260407, 2007.

[68] C. Roux, A. Emmert, A. Lupascu, T. Nirrengarten, G. Nogues, M. Brune, J.-M. Raimond, and S. Haroche. Bose-Einstein condensation on a superconducting atom chip. *Europhysics Letters*, 81:56004, 2008.

[69] V. Dikovsky, V. Sokolovsky, B. Zhang, C. Henkel, and R. Folman. Superconductive atom chips: advantages and challenges. *The European Physical Journal D*, 51:247, 2009.

[70] Yves Colombe, Tilo Steinmetz, Guilhem Dubois, Felix Linke, David Hunger, and Jakob Reichel. Strong atom-field coupling for Bose-Einstein condensates in an optical cavity on a chip. *Nature*, 450:272, 2007.

[71] S. Hofferberth, I. Lesanovsky, B. Fischer, T. Schumm, and J. Schmiedmayer. Non-equilibrium coherence dynamics in one-dimensional Bose gases. *Nature*, 449:324, 2007.

[72] Pascal Böhi, Max F. Riedel, Johannes Hoffrogge, Jakob Reichel, Theodor W. Hänsch, and Philipp Treutlein. Coherent manipulation of Bose-Einstein condensates with state-dependent microwave potentials on an atom chip. *Nature Physics*, 5:592, 2009.

[73] D. Heine, W. Rohringer, D. Fischer, M. Wilzbach, T. Raub, S. Loziczky, XiYuan Liu, S. Groth, B. Hessmo, and J. Schmiedmayer. A single-atom detector integrated on an atom chip: fabrication, characterization and application. *New Journal of Physics*, 12:095005, 2010.

[74] Max F. Riedel, Pascal Böhi, Yun Li, Theodor W. Hänsch, Alice Sinatra, and Philipp Treutlein. Atom-chip-based generation of entanglement for quantum metrology. *Nature*, 464:1170, 2010.

[75] A. Perrin, R Bücker, S Manz, T. Betz, C. Koller, T. Plisson, T. Schumm, and J. Schmiedmayer. Hanbury Brown and Twiss cor-

relations across the Bose-Einstein condensation threshold. *Nature Physics*, 8:195, 2012.

[76] C. J. Vale, B. Upcroft, M. J. Davis, N. R. Heckenberg, and H. Rubinsztein-Dunlop. Foil-based atom chip for Bose–Einstein condensates. *Journal of Physics B*, 37(14):2959, 2004.

[77] Ben Upcroft. *Atom Chips and Non-linear Dynamics in Macroscopic Atom Traps*. PhD thesis, Department of Physics, The University of Queensland, 2004.

[78] O. Vainio. Towards Bose-Einstein condensate on atom chip. MSc thesis, Department of Physics, University of Turku. 2003.

[79] C. V. Sukumar and D. M. Brink. Spin-flip transitions in a magnetic trap. *Physical Review A*, 56:2451, 1997.

[80] S. Gov, S. Shtrikman, and H. Thomas. 1D toy model for magnetic trapping. *American Journal of Physics*, 68:334, 2000.

[81] S. Dettmer, D. Hellweg, P. Ryytty, J. J. Arlt, W. Ertmer, K. Sengstock, D. S. Petrov, G. V. Shlyapnikov, H. Kreutzmann, L. Santos, and M. Lewenstein. Observation of phase fluctuations in elongated Bose-Einstein condensates. *Physical Review Letters*, 87:160406, 2001.

[82] W. Ketterle and N. J. van Druten. Evaporative cooling of trapped atoms. *Advances in Atomic, Molecular, and Optical Physics*, 37:181, 1996.

[83] Daniel A. Steck. Rubidium 87 D line data. http://steck.us/alkalidata, 2008.

[84] www.xmds.org.

[85] H.-J. Miesner, D. M. Stamper-Kurn, M. R. Andrews, D. S. Durfee, S. Inouye, and W. Ketterle. Bosonic stimulation in the formation of a Bose-Einstein condensate. *Science*, 279:1005, 1998.

[86] Stephan Ritter, Anton Öttl, Tobias Donner, Thomas Bourdel, Michael Köhl, and Tilman Esslinger. Observing the formation of long-range order during Bose-Einstein condensation. *Physical Review Letters*, 98:090402, 2007.

[87] M. Hugbart, J. A. Retter, A. F. Varón, P. Bouyer, A. Aspect, and M. J. Davis. Population and phase coherence during the growth of an elongated Bose-Einstein condensate. *Physical Review A*, 75:011602, 2007.

[88] D. M. Stamper-Kurn, H.-J. Miesner, A. P. Chikkatur, S. Inouye, J. Stenger, and W. Ketterle. Reversible formation of a Bose-Einstein condensate. *Physical Review Letters*, 81:2194, 1998.

[89] P. W. H. Pinkse, A. Mosk, M. Weidemüller, M. W. Reynolds, T. W. Hijmans, and J. T. M. Walraven. Adiabatically changing the phase-space density of a trapped Bose gas. *Physical Review Letters*, 78:991, 1997.

[90] R. Grimm, M. Weidemüller, and Y. B. Ovchinnikov. Optical dipole traps for neutral atoms. *Adcances in Atomic, Molecular and Optical Physics*, 42:95, 2000.

[91] Tino Weber, Jens Herbig, Michael Mark, Hanns-Christoph Nägerl, and Rudolf Grimm. Bose-Einstein condensation of cesium. *Science*, 299:232, 2003.

[92] J. Ahokas, J. Järvinen, G. V. Shlyapnikov, and S. Vasiliev. Clock shift in high field magnetic resonance of atomic hydrogen. *Physical Review Letters*, 101:263003, 2008.

[93] R. L. White and I. H. Solt. Multiple ferromagnetic resonance in ferrite spheres. *Physical Review*, 104:56, 1956.

[94] J. E. Mercereau and R. P. Feynman. Physical conditions for ferromagnetic resonance. *Physical Review*, 104:63, 1956.

[95] L. R. Walker. Magnetostatic modes in ferromagnetic resonance. *Physical Review*, 105:390, 1957.

[96] E. P. Bashkin. Spin waves in polarized paramagnetic gases. *JETP Letters*, 33:8, 1981.

[97] C. Lhuillier and F. Laloë. Transport properties in a spin polarized gas, I. *Le Journal de Physique*, 43:197, 1982.

[98] C. Lhuillier and F. Laloë. Transport properties in a spin polarized gas, II. *Le Journal de Physique*, 43:225, 1982.

[99] J. F. Dillon Jr. *Am. Phys. Soc. Ser. II*, 1:125, 1956.

[100] J. R. Eshbach and R. W. Damon. Surface magnetostatic modes and surface spin waves. *Physical Review*, 118:1208, 1960.

[101] B. A. Auld. Walker modes in large ferrite samples. *Journal of Applied Physics*, 31:1642, 1960.

[102] R. W. Damon and J. R. Eshbach. Magnetostatic modes of a ferromagnetic slab. *Journal of Physics and Chemistry of Solids*, 19:308, 1961.

[103] R. I. Joseph and E. Schlömann. Theory of magnetostatic modes in long, axially magnetized cylinders. *Journal of Applied Physics*, 32:1001, 1961.

[104] P. C. Fletcher and C. Kittel. Considerations on the propagation and generation of magnetostatic waves and spin waves. *Physical Review*, 120:2004, 1960.

[105] P. R. Emtage and Michael R. Daniel. Magnetostatic waves and spin waves in layered ferrite structures. *Physical Review B*, 29:212, 1984.

[106] R. W. Damon and H. van de Vaart. Propagation of magnetostatic spin waves at microwave frequencies in a normally-magnetized disk. *Journal of Applied Physics*, 36:3453, 1965.

[107] S. Bornmann, A. Schönecker, and W. Haubenreisser. Magnetostatic mode pattern and mode spectrum analysis in finite ferromagnetic circular disks. *phys. stat. sol*, 11:207, 1972.

[108] Masanori Koshiba and Yi Long. Finite-element analysis of magnetostatic wave propagation in a YIG film of finite dimension. *IEEE Transactions on Microwave Theory and Techniques*, 37:1768, 1989.

[109] D. D. Osheroff and M. C. Cross. Magnetostatic modes in highly polarized solid helium-three. *Physical Review Letters*, 59:94, 1987.

[110] T. Ueda, Y. Ueda, H. Shimasaki, and M. Tsutsumi. Numerical analysis of nonlinear magnetostatic wave propagation by finite-element method. *IEEE Transactions on Magnetics*, 39:3157, 2003.

[111] R. Zivieri and R. L. Stamps. Theory of spin wave modes in tangentially magnetized thin cylindrical dots, a variational approach. *Physical Review B*, 73:144422, 2006.

[112] K. Rivkin, Xy Wentao, L. E. De Long, V. V. Metlushko, B. Ilic, and J. B. Ketterson. Analysis of ferromagnetic resonance response of square arrays of permalloy nanodots. *Journal of Magnetism and Magnetic Materials*, 309:317, 2007.

[113] Rodrigo Arias and D. L. Mills. Theory of spin excitations and the microwave response of cylindrical ferromagnetic nanowires. *Physical Review B*, 63:134439, 2001.

[114] J.-P. Bouchaud and C. Lhuillier. Hyperfine and electronic spin waves in atomic hydrogen: the role of the spin exchange process. *Le Journal de Physique*, 46:1781, 1985.

[115] D. M. Lee. Spin waves in spin polarized hydrogen. *Japanese Journal of Applied Physics*, 26:1841, 1987.

[116] Nicholas Pierre Bigelow. *Spin Wave Spectroscopy of Atomic Hydrogen*. PhD thesis, Cornell University, 1989.

[117] A. J. Leggett. Spin diffusion and spin echoes in liquid 3He at low temperature. *Journal of Physics C*, 3:448, 1970.

[118] C. Lhuillier. Transport properties in a spin polarized gas, III. *Le Journal de Physique*, 44:1, 1983.

[119] P. J. Nacher, G. Tastevin, M. Leduc, S. B. Crampton, and F. Laloë. Spin rotation effects and spin waves in gaseous ^{3}He↑. *Journal de Physique Lettres*, 45:L−441, 1984.

[120] G. Tastevin, P. J. Nacher, M. Leduc, and F. Laloë. Direct detection of spin waves in gaseous ^{3}He↑. *Journal de Physique Lettres*, 46:L−249, 1985.

[121] W. J. Gully and W. J. Mullin. Observation of spin rotation effects in polarized ^{3}He-^{4}He mixtures. *Physical Review Letters*, 52:1810, 1984.

[122] B. R. Johnson, J. S. Denker, N. P. Bigelow, L. P. Lévy, J. H. Freed, and D. M. Lee. Observation of nuclear spin waves in spin-polarized atomic hydrogen gas. *Physical Review Letters*, 52:1508, 1984.

[123] Laurent P. Lévy and Andrei E. Ruckenstein. Collective spin oscillations in spin-polarized gases: Spin-polarized hydrogen. *Physical Review Letters*, 52:1512, 1984.

[124] J. M. V. A. Koelman, H. J. M. F. Noteborn, L. P. H. de Goey, and B. J. Verhaar. Spin waves in H↓ adsorbed on a superfluid ^{4}He film. *Physical Review B*, 32:7195, 1985.

[125] J.-P. Bouchaud and C. Lhuillier. Convective instabilities in spin-polarized gases. *Physics Letters A*, 116:99, 1986.

[126] N. P. Bigelow, J. H. Freed, and D. M. Lee. Nuclear-spin waves in polarized atomic hydrogen gas: Temperature and density dependence in the hydrodynamic and Knudsen regimes. *Physical Review Letters*, 63:1609, 1989.

[127] H. J. Lewandowski, D. M. Harber, D. L. Whitaker, and E. A. Cornell. Observation of anomalous spin-state segregation in a trapped ultracold vapor. *Physical Review Letters*, 88:070403, 2002.

[128] M. Ö. Oktel and L. S. Levitov. Internal waves and synchronized precession in a cold vapor. *Physical Review Letters*, 88:230403, 2002.

[129] J. N. Fuchs, D. M. Gangardt, and F. Laloë. Internal state conversion in ultracold gases. *Physical Review Letters*, 88:230404, 2002.

[130] J. E. Williams, T. Nikuni, and Charles W. Clark. Longitudinal spin waves in a dilute Bose gas. *Physical Review Letters*, 88:230405, 2002.

[131] J. M. McGuirk, H. J. Lewandowski, D. M. Harber, T. Nikuni, J. E. Williams, and E. A. Cornell. Spatial resolution of spin waves in an ultracold gas. *Physical Review Letters*, 89:090402, 2002.

[132] X. Du, L. Luo, B. Clancy, and J. E. Thomas. Observation of anomalous spin segregation in a trapped Fermi gas. *Physical Review Letters*, 101:150401, 2008.

[133] F. Piéchon, J. N. Fuchs, and F. Laloë. Cumulative identical spin rotation effects in collisionless trapped atomic gases. *Physical Review Letters*, 102:215301, 2009.

[134] Stefan S. Natu and Erich J. Mueller. Anomalous spin segregation in a weakly interacting two-component Fermi gas. *Physical Review A*, 79:051601, 2009.

[135] X. Du, Y. Zhang, J. Petrica, and J. E. Thomas. Controlling spin current in a trapped Fermi gas. *Physical Review Letters*, 103:010401, 2009.

[136] C. Deutsch, F. Ramirez-Martinez, C. Lacroûte, F. Reinhard, T. Schneider, J. N. Fuchs, F. Piéchon, F. Laloë, J. Reichel, and P. Rosenbusch. Spin self-rephasing and very long coherence times in a trapped atomic ensemble. *Physical Review Letters*, 105:020401, 2010.

[137] J. M. McGuirk. Spin transport in coupled spinor Bose gases. *Physical Review A*, 82:011612(R), 2010.

[138] J. M. McGuirk and L. F. Zajiczek. Optical excitation of nonlinear spin waves. *New Journal of Physics*, 12:103020, 2010.

[139] L. R. Corruccini, D. D. Osheroff, D. M. Lee, and R. C. Richardson. Spin-wave phenomena in liquid ^{3}He systems. *Journal of Low Temperature Physics*, 8:229, 1972.

[140] N. Masuhara, D. Candela, D. O. Edwards, R. F. Hoyt, H. N. Scholz, D. S. Sherrill, and R. Combescot. Collisionless spin waves in liquid ^{3}He. *Physical Review Letters*, 53:1168, 1984.

[141] J. R. Owers-Bradley, H. Chocolacs, R. M. Mueller, Ch. Buchal, M. Kubota, and F. Pobell. Spin waves in liquid ^{3}He-^{4}He mixtures. *Physical Review Letters*, 51:2120, 1983.

[142] D. Candela, N. Masuhara, D. S. Sherrill, and D. O. Edwards. Collisionless spin waves in normal and superfluid ^{3}He. *Journal of Low Temperature Physics*, 63:369, 1986.

[143] A. S. Borovik-Romanov, Yu. M. Bunkov, V. V. Dmitriev, and Yu. M. Mukharskii. Long-lived induction signal in superfluid ^{3}He-B. *JETP Letters*, 40:1033, 1984.

[144] I. A. Fomin. Long-lived induction signal and spatially nonuniform spin preceession in ^{3}He-B. *JETP Letters*, 40:1036, 1984.

[145] Yuriy M. Bunkov and Grigory E. Volovik. Bose-Einstein condensation of magnons in superfluid ^{3}He. *Journal of Low Temperature Physics*, 150:135, 2008.

[146] Yuriy M. Bunkov and Grigory E. Volovik. Magnon Bose-Einstein condensation and spin superfluidity. *Journal of Physics: Condensed Matter*, 22:164210, 2010.

[147] Sergei Vasilyev, Jarno Järvinen, Esa Tjukanoff, Alexander Kharitonov, and Simo Jaakkola. Cryogenic 2 mm wave electron spin resonance spectrometer with application to atomic hydrogen gas below 100 mK. *Review of Scientific Instruments*, 75:94, 2004.

[148] Craig T. Van Degrift. Tunnel diode oscillator for 0.001 ppm measurements at low temperatures. *Review of Scientific Instruments*, 46:599, 1975.

[149] S. G. Gevorgyan, G. D. Movsesyan, A. A. Movsisyan, V. T. Tatoyan, and H. G. Shirinyan. Modeling of tunnel diode oscillators and their use for some low temperature investigations. *Review of Scientific Instruments*, 69:2550, 1998.

[150] Janne Ahokas. *Magnetic Resonance Experiments with Atomic Hydrogen*. PhD thesis, University of Turku, Ann. Univ. Turku. Ser. A I, No. 412, 2010.